cGAS-like receptors sense RNA and control 3'2'-cGAMP signalling in Drosophila

Kailey M. Slavik, Benjamin R. Morehouse, Adelyn E. Ragucci, Wen Zhou,
Xianlong Ai, Yuqiang Chen, Lihua Li, Ziming Wei, Heike Bähre, Martin
König, et al.

cGAS-like receptors control RNA sensing and 3′2′-cGAMP antiviral signaling in Drosophila

Kailey M. Slavik[1,2], Benjamin R. Morehouse[1,2], Adelyn E. Ragucci[1,2], Wen Zhou[1,2,9], Xianlong Ai[3], Yuqiang Chen[3], Lihua Li[3], Ziming Wei[3], Heike Bähre[4], Martin König[4], Roland Seifert[4,5], Amy S. Y. Lee[2,6], Hua Cai[3], Jean-Luc Imler[3,7], Philip J. Kranzusch[1,2,8*]

[1] Department of Microbiology, Harvard Medical School, Boston, MA 02115, USA

[2] Department of Cancer Immunology and Virology, Dana-Farber Cancer Institute, Boston, MA 02115, USA

[3] Sino-French Hoffmann Institute, State Key Laboratory of Respiratory Disease, School of Basic Medical Science, Guangzhou Medical University, Guangzhou, 511436, China.

[4] Research Core Unit Metabolomics, Hannover Medical School, 30625 Hannover, Germany

[5] Hannover Medical School, Institute of Pharmacology, Carl-Neuberg-Str. 1, 30625 Hannover, Germany

[6] Department of Cell Biology, Harvard Medical School, Boston, MA 02115, USA

[7] Université de Strasbourg, CNRS UPR9022, 67084 Strasbourg, France

[8] Parker Institute for Cancer Immunotherapy at Dana-Farber Cancer Institute, Boston, MA 02115, USA

[9] Present address: School of Life Sciences, Southern University of Science and Technology, Shenzhen, Guangdong, China

*Correspondence: philip_kranzusch@dfci.harvard.edu

Cyclic GMP–AMP synthase (cGAS) is a cytosolic DNA sensor that produces the second messenger 2′3′-cGAMP and controls activation of innate immunity in mammalian cells[1-5]. Animal genomes typically encode multiple proteins with predicted homology to cGAS[6-12], but the function of these uncharacterized enzymes is unknown. Here we show that cGAS-like receptors (cGLRs) are innate immune sensors capable of recognizing divergent molecular patterns and catalyzing synthesis of distinct nucleotide second messenger signals. Crystal structures of human and insect cGLRs reveal a nucleotidyltransferase signaling core shared with cGAS and a diversified primary ligand-binding surface modified with significant insertions and deletions. We demonstrate that cGLR surface remodeling enables altered ligand specificity and use a forward biochemical screen to identify cGLR1 as a double-stranded RNA sensor in the model organism *Drosophila melanogaster*. Surprisingly, RNA recognition activates *Drosophila* cGLR1 to synthesize the novel product cG[3′–5′]pA[2′–5′]p (3′2′-cGAMP). A crystal structure of *Drosophila* Stimulator of Interferon Genes (STING) in complex with 3′2′-cGAMP explains selective isomer recognition and we demonstrate that 3′2′-cGAMP induces an enhanced antiviral state *in vivo* that protects from viral infection. Similar to radiation of Toll-like receptors in pathogen immunity, our results establish cGLRs as a diverse family of metazoan pattern recognition receptors.

To define the function of cGAS-like enzymes in animals, we screened predicted cGAS-homologs for suitability in structural analysis and determined a 2.4 Å crystal structure of the human protein MB21D2 (hMB21D2; C3orf59) and a 1.6 Å crystal structure of a protein from the beetle species *Tribolium castaneum* (Genbank XP_969398.1) (Supplementary Table 1). Despite primary sequence divergence, the hMB21D2 and *T. castaneum* XP_969398.1 structures each reveal close homology to human cGAS with a shared bi-lobed architecture, caged nucleotidyltransferase core, Gly-[Gly/Ser]-activation loop, and putative catalytic triad (Fig. 1a, Extended Data Fig. 1). In human cGAS, the primary ligand binding surface is a long groove on

27 the back of the enzyme formed by the α-helix spine and a Zn-ribbon motif that is essential for

28 recognition of double-stranded DNA[3,13-17]. A conserved groove is present in both the hMB21D2

29 and *T. castaneum* XP_969398.1 structures (Fig. 1a) but is notably distinguished by the absence

30 of a Zn-ribbon and the insertion of a C-terminal α-helix in hMB21D2 (Fig. 1b). We hypothesized

31 that the remodeling of this groove controls the detection of distinct activating ligands. The

32 hMB21D2 surface is overall neutral with no obvious capacity to coordinate nucleic acid and no

33 enzyme activity was detected in the presence of potential activating ligands (Extended Data Fig.

34 1d,e). In contrast to hMB21D2, the surface of *T. castaneum* XP_969398.1 shares highly

35 conserved basic residues with human cGAS (Fig. 1a) and we therefore tested this enzyme with

36 candidate DNA and RNA ligands. Remarkably, we observed that *T. castaneum* XP_969398.1 is

37 activated to synthesize a nucleotide product in response to recognition of double-stranded RNA

38 (dsRNA) (Fig. 1c). Despite exhibiting a clear difference in ligand-specificity, analysis of all related

39 structures in the Protein Data Bank confirms that *T. castaneum* XP_969398.1 is a close homolog

40 of mammalian cGAS and is distinct from previously characterized RNA sensors including

41 oligoadenylate synthase 1 (Extended Data Fig. 1f)[18,19]. Together, these results establish the

42 existence of cGAS-like Receptors (cGLRs) in animals and demonstrate that remodeling of a

43 primary ligand-binding surface enables the recognition of divergent molecular patterns.

44   To identify additional cGLRs that respond to dsRNA, we used the *T. castaneum* cGLR

45 (*Tc*-cGLR) sequence to search for predicted cGAS homologs in species related to the model

46 organism *Drosophila melanogaster*. We identified 153 cGLR genes across 42 species in the order

47 *Diptera*, which cluster into distinct clades designated 1–5 (Fig. 2a; Supplementary Table 2).

48 *Drosophila* exhibit a remarkable radiation of cGLR genes with individual species encoding

49 between three and seven predicted enzymes (Extended Data Fig. 2a). In a systematic

50 biochemical screen, we purified and tested 53 recombinant cGLR proteins and identified active

51 enzymes from the species *Lucilia cuprina*, *Drosophila eugracilis*, *Drosophila erecta*, and

52 *Drosophila simulans* (Extended Data Figs. 2b–f, 3a)*.* Similar to *Tc*-cGLR, each active *Diptera*

53   enzyme specifically responds to dsRNA indicating that cGLR-based recognition of RNA is

54   conserved across diverse insect species (Fig. 2b; Extended Data Fig. 4a).

55   The *D. simulans* enzyme identified in our screen shares 91% sequence identity with the

56   protein product of the uncharacterized *D. melanogaster* gene *CG12970*. We purified recombinant

57   *D. melanogaster* CG12970 and found that it synthesizes a nucleotide product specifically in the

58   presence of dsRNA and we therefore named this gene *cGAS-like Receptor 1* (*Dm-cGLR1*) (Fig.

59   2c). To understand how dsRNA activates *Drosophila* cGLR1, we analyzed the molecular

60   determinants for enzymatic activity *in vitro.* We observed that *D. simulans* cGLR1 (*Ds*-cGLR1)

61   and *Dm*-cGLR1 recognize long >30 bp dsRNA with no preference for 5′ RNA phosphorylation

62   (Fig. 2d; Extended Data Fig. 4b,c). Notably, activation of *Dm*-cGLR1 and *Ds*-cGLR1 requires

63   dsRNA ligands that exceed the length of 21–23 bp RNA molecules commonly produced during

64   RNA interference (RNAi) in *Drosophila*, suggesting specific avoidance of self-recognition[20-22]. *Ds*-

65   cGLR1 selectively binds dsRNA and forms a higher-order complex that is dependent on dsRNA

66   length, similar to condensate formation previously observed with hcGAS recognition of dsDNA

67   (Fig. 2e; Extended Data Fig. 5)[23-25]. Using the *Tc*-cGLR and human cGAS–DNA structures as a

68   template[17], we modeled interactions between *Drosophila* cGLR1 and dsRNA (Fig. 2f). Single

69   glutamate substitutions to the conserved basic residues R41, R259, and K269 within the predicted

70   *Ds*-cGLR1 ligand binding surface significantly diminish dsRNA-stimulated activity (Fig. 2g;

71   Extended Data Fig. 3). We ectopically expressed *Dm*-cGLR1 or *Ds*-cGLR1 in human cells and

72   observed that expression is sufficient to enable dsRNA sensing and drive activation of a STING-

73   dependent immune response (Fig. 2h; Extended Data Fig. 4e). *Dm*-cGLR1 and *Ds*-cGLR1

74   signaling in cells is strictly dependent on dsRNA stimulation and mutations to the enzyme catalytic

75   site or conserved ligand-binding surface disrupt signaling and prevent downstream STING

76   activation (Fig. 2h; Extended Data Fig. 3f). Together, these data demonstrate that insect cGLRs

77   and human cGAS use a shared mechanism of ligand detection and reveal that *Dm*-cGLR1 can

78   function as a foreign RNA sensor.

79   A role in sensing foreign RNA suggests that the function of *Dm*-cGLR1 is to control

80   activation of a downstream immune response in *Drosophila*. In human cells, cGAS catalyzes

81   production of the nucleotide second messenger 2′3′-cGAMP (cG[2′–5′]pA[3′–5′]p) that contains a

82   non-canonical 2′–5′ phosphodiester linkage required for potent activation of immune signaling[2-5].

83   To determine how *Dm*-cGLR1 controls cellular signaling, we purified the nucleotide reaction

84   product for direct comparison to 2′3′-cGAMP. Surprisingly, *Dm*-cGLR1 synthesizes a nucleotide

85   product that exhibits a C18 chromatography migration profile distinct from 2′3′-cGAMP and all

86   previously known naturally occurring cyclic dinucleotide (CDN) signals (Fig. 3a; Extended Data

87   Fig. 6). Production of this nucleotide signal is conserved in *Diptera* with *Ds*-cGLR1, *Lc*-cGLR, and

88   *Deu*-cGLR reactions each synthesizing the same major reaction product (Extended Data Fig. 6a).

89   Using nucleobase-specific labeling and nuclease digestion of the *Dm*-cGLR1 product we

90   observed a 3′−5′-linkage connected to an adenosine phosphate and a protected 2′−5′-linkage

91   connected to a guanosine phosphate suggesting the existence of a mixed-linkage cyclic GMP–

92   AMP species (Fig. 3b). We verified these findings with comparative high performance liquid

93   chromatography and tandem mass-spectrometry profiling against a chemically synthesized

94   standard and confirmed that the shared *Diptera* cGLR product is the novel isomer 3′2′-cGAMP

95   (cG[3′–5′]pA[2′–5′]p) (Figs. 3a,b; Extended Data Figs. 6a,b).

96   *Dm*-cGLR1 synthesizes 3′2′-cGAMP in a two-step reaction through production of the linear

97   intermediate pppA[2′–5′]pG and uses an opposite nucleobase reaction order compared to human

98   cGAS (Extended Data Fig. 7a)[2,3,26]. We next used mass-spectrometry to further analyze each

99   lysate sample from our screen of recombinant dipteran cGLR proteins. 3′2′-cGAMP was detected

100   as a main reaction product from 15 *Diptera* cGLRs including active enzymes from each sub-group

101   within Clade 5 of the insect cGLR phylogeny (Fig. 3c, Extended Data Fig. 6c). cGLRs clustered

102   within Clade 5 collectively represent 41 species suggesting widespread conservation of 3′2′-

103   cGAMP-sigaling in *Diptera*. Interestingly, the beetle enzyme *Tc*-cGLR synthesizes 2′3′-cGAMP,

104   supporting that 2′3′-cGAMP is an ancestral signaling molecule in metazoans and that 3′2′-

105   cGAMP-signaling is a recent adaptation in flies (Fig. 3d; Extended Data Fig. 6a)[10,27,28]. Insect and

106   mammalian viruses encode 2′3′-cGAMP-specific nucleases named poxins that allow evasion of

107   cGAS-STING immune responses[29,30]. Remarkably, 3′2′-cGAMP is protected from poxin cleavage

108   (Extended Data Fig. 7b–d), indicating that an isomeric switch in phosphodiester linkage specificity

109   endows *Drosophila* with a signaling pathway resistant to a major form of viral immune evasion.

110   *Drosophila* STING (dSTING) is known to function as a cyclic dinucleotide receptor *in*

111   *vivo*[31-34], but an endogenous nucleotide second messenger has not previously been identified.

112   We therefore developed an *in vitro* thermo-fluor binding assay to analyze the ability of dSTING to

113   recognize specific CDNs. dSTING preferentially forms a thermo-stable complex with 3′2′-cGAMP

114   and exhibits no detectable complex formation with 2′3′-cGAMP or other CDNs *in vitro* (Fig. 4a;

115   Extended Data Fig. 8b,c). Using direct delivery of CDNs to permeabilized cells, we confirmed that

116   dSTING preferentially responds to 3′2′-cGAMP in the cellular environment (Extended Data Fig.

117   8d). To define the mechanism of selective 3′2′-cGAMP recognition, we next determined a 2.0 Å

118   crystal structure of the *D. eugracilis* STING CDN-binding domain in complex with 3′2′-cGAMP

119   (Fig. 4b). dSTING adopts a highly conserved V-shaped homodimeric architecture with a deep

120   central pocket that binds 3′2′-cGAMP. The dSTING–3′2′-cGAMP structure reveals a tightly

121   "closed" conformation with dSTING protomers positioned 36 Å apart, similar to the closed

122   conformation of human STING bound to 2′3′-cGAMP (Extended Data Fig. 8e)[5,35]. Each

123   nucleobase of 3′2′-cGAMP is stacked between dSTING Y164 and R234, and E257 specifically

124   coordinates the 3′2′-cGAMP guanosine N2 position (Fig. 4c,d). In human STING, high-affinity

125   recognition of 2′3′-cGAMP requires readout of the 2′–5′ phosphodiester linkage by R232 in the β-

126   strand lid[5,35]. In dSTING, the equivalent R229 makes no contact with either phosphodiester bond.

127   Instead, R229 is repositioned to extend outward from the ligand binding pocket by the deletion of

128   a single lid residue and the formation of a salt bridge with E267 on the opposing protomer,

129   explaining the diminished affinity of dSTING for 2′3′-cGAMP (Fig. 4c,e). Additionally, a key

130   asparagine substitution N159 in dSTING extends across the binding pocket to coordinate the

131 adenosine 3′ OH in 3′2′-cGAMP and directly replaces the human STING S162 residue that

132 contacts the guanosine 3′ OH in 2′3′-cGAMP (Fig. 4f). We tested a panel of dSTING mutant

133 proteins and confirmed that mutations to each coordinating residue disrupt dSTING–3′2′-cGAMP

134 complex formation (Extended Data Fig. 8i). The unique ligand-binding pocket adaptations

135 observed in the dSTING–3′2′-cGAMP structure are widely conserved in *Diptera* and together

136 explain a mechanism for how specific 3′2′-cGAMP-dependent signaling drives STING activation.

137   To determine how *Dm*-cGLR1–3′2′-cGAMP–STING signaling controls immune responses

138 *in vivo*, we next injected 3′2′-cGAMP into *D. melanogaster* to directly monitor the dSTING

139 response. 3′2′-cGAMP potently induces the expression of *dSTING* and three other STING-

140 regulated genes in a dose-dependent manner (Fig 5a; Extended Data Fig. 9). Notably, 3′2′-

141 cGAMP-dependent signaling through dSTING is significantly more potent than the response

142 triggered by injection of the bacterial CDN signal 3′3′-c-di-GMP (Fig 5a; Extended Data Fig. 9e–

143 k). Genetic mutations to *dSTING* and the NF-κB homolog *Relish* ablate 3′2′-cGAMP-induced

144 responses, demonstrating that signaling is dependent upon each downstream pathway

145 component (Fig. 5a, Extended Data Fig. 9e–k). We challenged flies with viral infection and

146 observed that 3′2′-cGAMP markedly suppresses the replication of two unrelated RNA viruses,

147 *Drosophila* C virus (*Dicistroviridae*), a natural *Drosophila* pathogen, and vesicular stomatitis virus

148 (*Rhabdoviridae*) (Figs. 5b,c; Extended Data Fig. 10a,b). 3′2′-cGAMP activation of antiviral

149 immunity is strictly dependent on dSTING and results in a response that significantly delays

150 pathogen-mediated mortality (Figs. 5b,c; Extended Data Fig. 10a,b). Direct comparison of the

151 protective effects against DCV infection demonstrates that the endogenous signal 3′2′-cGAMP

152 exhibits greater antiviral potency than 2′3′-cGAMP. 3′2′-cGAMP more robustly suppresses RNA

153 viral loads and extends animal survival (Fig. 5d; Extended data Fig. 10c,d), revealing that the

154 dSTING antiviral signaling axis is preferentially activated by 3′2′-cGAMP *in vivo*. Together, these

155 results demonstrate that 3′2′-cGAMP is an antiviral nucleotide second messenger in *D.*

156   *melanogaster* and establish a novel cGLR–STING–NF-κB axis that protects animals from viral

157   replication.

158   Along with cGAS recognition of dsDNA, the discovery of animal cGLR dsRNA sensors

159   establishes a diverse class of pattern recognition receptors conserved throughout metazoans.

160   Divergent structural homologs of cGAS in humans and insects demonstrate that cGLRs constitute

161   a rapidly evolving family of proteins in which remodeling of a shared primary binding surface

162   enables the detection of diverse ligands. Our characterization of the mechanism of *Drosophila*

163   cGLR1 activation shows that cGLRs function as direct sensors of pathogen-associated molecular

164   patterns and synthesize distinct second messengers to control a conserved downstream signaling

165   axis. *Drosophila* were previously thought to respond to foreign nucleic acid exclusively through

166   RNAi and direct cleavage of pathogen RNA[21,22]. *Drosophila* cGLR1 reveals a parallel signaling

167   system for sensing foreign RNA and directing an inducible immune response through STING.

168   Synthesis of the novel second messenger 3′2′-cGAMP by *Drosophila* cGLR1 and selective

169   recognition by dSTING provides the first evidence that metazoans use CDNs beyond 2′3′-cGAMP

170   as endogenous second messengers and highlights the evolutionary plasticity of cGLR signaling.

171   Our structural analysis also reveals that the human cGLR MB21D2 is competent for nucleotide

172   second messenger synthesis and has a remodeled ligand-binding groove likely adapted for

173   detection of an unknown stimulus. Together with the known high frequency of hMB21D2 mutation

174   in cancer[37,38], these results support a more extensive role for cGLR signaling in human biology.

175   The existence of multiple unique cGLRs encoded within a single species (Extended Data Fig. 2a)

176   suggests a model in which the cGLR signaling scaffold is harnessed to detect a number of distinct

177   stimuli (Fig. 5e). In support of this conclusion, Hartmann, Imler, Cai and colleagues identify cGLR2

178   as a second functional cGLR in *Drosophila* and demonstrate *in vivo* that cGLR1 and cGLR2 have

179   distinct functions in *Drosophlia* immunity[36]. Together, our results define cGLRs as receptors in

180   animal cells capable of detecting diverse pathogen-associated molecular patterns and dictating

181   response to the foreign environment.

References

183   1   Sun, L., Wu, J., Du, F., Chen, X. & Chen, Z. J. Cyclic GMP-AMP synthase is a cytosolic DNA sensor that
184   activates the type I interferon pathway. *Science* (2013) **339**, 786-791. PMC3863629.

185   2   Ablasser, A., Goldeck, M., Cavlar, T., Deimling, T., Witte, G., Rohl, I., Hopfner, K. P., Ludwig, J. & Hornung,
186   V. cGAS produces a 2'-5'-linked cyclic dinucleotide second messenger that activates STING. *Nature* (2013)
187   **498**, 380-384. PMC4143541.

188   3   Gao, P., Ascano, M., Wu, Y., Barchet, W., Gaffney, B. L., Zillinger, T., Serganov, A. A., Liu, Y., Jones, R. A.,
189   Hartmann, G., Tuschl, T. & Patel, D. J. Cyclic [G(2',5')pA(3',5')p] is the metazoan second messenger produced
190   by DNA-activated cyclic GMP-AMP synthase. *Cell* (2013) **153**, 1094-1107. PMC4382009.

191   4   Diner, E. J., Burdette, D. L., Wilson, S. C., Monroe, K. M., Kellenberger, C. A., Hyodo, M., Hayakawa, Y.,
192   Hammond, M. C. & Vance, R. E. The innate immune DNA sensor cGAS produces a noncanonical cyclic
193   dinucleotide that activates human STING. *Cell Rep* (2013) **3**, 1355-1361. PMC3706192.

194   5   Zhang, X., Shi, H., Wu, J., Zhang, X., Sun, L., Chen, C. & Chen, Z. J. Cyclic GMP-AMP containing mixed
195   phosphodiester linkages is an endogenous high-affinity ligand for STING. *Mol Cell* (2013) **51**, 226-235.
196   PMC3808999.

197   6   Kranzusch, P. J. cGAS and CD-NTase enzymes: structure, mechanism, and evolution. *Curr Opin Struct Biol*
198   (2019) **59**, 178-187. PMC7127440.

199   7   Wu, J. & Chen, Z. J. Innate immune sensing and signaling of cytosolic nucleic acids. *Annu Rev Immunol*
200   (2014) **32**, 461-488

201   8   Burroughs, A. M., Zhang, D., Schaffer, D. E., Iyer, L. M. & Aravind, L. Comparative genomic analyses reveal
202   a vast, novel network of nucleotide-centric systems in biological conflicts, immunity and signaling. *Nucleic*
203   *Acids Res* (2015) **43**, 10633-10654. PMC4678834.

204   9   Wu, X., Wu, F. H., Wang, X., Wang, L., Siedow, J. N., Zhang, W. & Pei, Z. M. Molecular evolutionary and
205   structural analysis of the cytosolic DNA sensor cGAS and STING. *Nucleic Acids Res* (2014) **42**, 8243-8257.
206   PMC4117786.

207   10   Kranzusch, P. J., Wilson, S. C., Lee, A. S., Berger, J. M., Doudna, J. A. & Vance, R. E. Ancient Origin of
208   cGAS-STING Reveals Mechanism of Universal 2',3' cGAMP Signaling. *Mol Cell* (2015) **59**, 891-903.
209   PMC4575873.

210   11   Whiteley, A. T., Eaglesham, J. B., de Oliveira Mann, C. C., Morehouse, B. R., Lowey, B., Nieminen, E. A.,
211   Danilchanka, O., King, D. S., Lee, A. S. Y., Mekalanos, J. J. & Kranzusch, P. J. Bacterial cGAS-like enzymes
212   synthesize diverse nucleotide signals. *Nature* (2019) **567**, 194-199. PMC6544370.

213   12   de Oliveira Mann, C. C., Kiefersauer, R., Witte, G. & Hopfner, K. P. Structural and biochemical characterization
214   of the cell fate determining nucleotidyltransferase fold protein MAB21L1. *Sci Rep* (2016) **6**, 27498.
215   PMC4897736.

216   13   Civril, F., Deimling, T., de Oliveira Mann, C. C., Ablasser, A., Moldt, M., Witte, G., Hornung, V. & Hopfner, K.
217   P. Structural mechanism of cytosolic DNA sensing by cGAS. *Nature* (2013) **498**, 332-337. PMC3768140.

218   14   Kranzusch, P. J., Lee, A. S., Berger, J. M. & Doudna, J. A. Structure of human cGAS reveals a conserved
219   family of second-messenger enzymes in innate immunity. *Cell Rep* (2013) **3**, 1362-1368. PMC3800681.

220   15   Li, X., Shu, C., Yi, G., Chaton, C. T., Shelton, C. L., Diao, J., Zuo, X., Kao, C. C., Herr, A. B. & Li, P. Cyclic
221   GMP-AMP synthase is activated by double-stranded DNA-induced oligomerization. *Immunity* (2013) **39**, 1019-
222   1031. PMC3886715.

223   16   Zhang, X., Wu, J., Du, F., Xu, H., Sun, L., Chen, Z., Brautigam, C. A., Zhang, X. & Chen, Z. J. The cytosolic
224   DNA sensor cGAS forms an oligomeric complex with DNA and undergoes switch-like conformational changes
225   in the activation loop. *Cell Rep* (2014) **6**, 421-430. PMC3969844.

226   17   Zhou, W., Whiteley, A. T., de Oliveira Mann, C. C., Morehouse, B. R., Nowak, R. P., Fischer, E. S., Gray, N.
227   S., Mekalanos, J. J. & Kranzusch, P. J. Structure of the Human cGAS-DNA Complex Reveals Enhanced
228   Control of Immune Surveillance. *Cell* (2018) **174**, 300-311 e311. PMC6084792.

229   18   Lohofener, J., Steinke, N., Kay-Fedorov, P., Baruch, P., Nikulin, A., Tishchenko, S., Manstein, D. J. & Fedorov,
230   R. The Activation Mechanism of 2'-5'-Oligoadenylate Synthetase Gives New Insights Into OAS/cGAS Triggers
231   of Innate Immunity. *Structure* (2015) **23**, 851-862

232   19   Donovan, J., Dufner, M. & Korennykh, A. Structural basis for cytosolic double-stranded RNA surveillance by
233   human oligoadenylate synthetase 1. *Proc Natl Acad Sci U S A* (2013) **110**, 1652-1657. PMC3562804.

234   20   Ghildiyal, M. & Zamore, P. D. Small silencing RNAs: an expanding universe. *Nat Rev Genet* (2009) **10**, 94-
235   108. PMC2724769.

236   21   Guo, Z., Li, Y. & Ding, S. W. Small RNA-based antimicrobial immunity. *Nat Rev Immunol* (2019) **19**, 31-44

237   22   Schneider, J. & Imler, J. L. Sensing and signalling viral infection in drosophila. *Dev Comp Immunol* (2021)
238   **117**, 103985

239   23   Du, M. & Chen, Z. J. DNA-induced liquid phase condensation of cGAS activates innate immune signaling.
240   *Science* (2018) **361**, 704-709

241 24 Xie, W., Lama, L., Adura, C., Tomita, D., Glickman, J. F., Tuschl, T. & Patel, D. J. Human cGAS catalytic
242   domain has an additional DNA-binding interface that enhances enzymatic activity and liquid-phase
243   condensation. *Proc Natl Acad Sci U S A* (2019) **116**, 11946-11955. PMC6575157.
244 25 Zhou, W., Mohr, L., Maciejowski, J. & Kranzusch, P. J. cGAS phase separation inhibits TREX1-mediated DNA
245   degradation and enhances cytosolic DNA sensing. *Mol Cell* (2021) **81**, DOI 10.1016/j.molcel.2021.1001.1024.
246 26 Kranzusch, P. J., Lee, A. S. Y., Wilson, S. C., Solovykh, M. S., Vance, R. E., Berger, J. M. & Doudna, J. A.
247   Structure-guided reprogramming of human cGAS dinucleotide linkage specificity. *Cell* (2014) **158**, 1011-1021.
248   PMC4157622.
249 27 Gui, X., Yang, H., Li, T., Tan, X., Shi, P., Li, M., Du, F. & Chen, Z. J. Autophagy induction via STING trafficking
250   is a primordial function of the cGAS pathway. *Nature* (2019) **567**, 262-266
251 28 Morehouse, B. R., Govande, A. A., Millman, A., Keszei, A. F. A., Lowey, B., Ofir, G., Shao, S., Sorek, R. &
252   Kranzusch, P. J. STING cyclic dinucleotide sensing originated in bacteria. *Nature* (2020) **586**, 429-433.
253   PMC7572726.
254 29 Eaglesham, J. B., Pan, Y., Kupper, T. S. & Kranzusch, P. J. Viral and metazoan poxins are cGAMP-specific
255   nucleases that restrict cGAS-STING signalling. *Nature* (2019) **566**, 259-263. PMC6640140.
256 30 Eaglesham, J. B., McCarty, K. L. & Kranzusch, P. J. Structures of diverse poxin cGAMP nucleases reveal a
257   widespread role for cGAS-STING evasion in host-pathogen conflict. *Elife* (2020) **9**. PMC7688311.
258 31 Goto, A., Okado, K., Martins, N., Cai, H., Barbier, V., Lamiable, O., Troxler, L., Santiago, E., Kuhn, L., Paik,
259   D., Silverman, N., Holleufer, A., Hartmann, R., Liu, J., Peng, T., Hoffmann, J. A., Meignin, C., Daeffler, L. &
260   Imler, J. L. The Kinase IKKbeta Regulates a STING- and NF-kappaB-Dependent Antiviral Response Pathway
261   in Drosophila. *Immunity* (2018) **49**, 225-234 e224. PMC6267954.
262 32 Liu, Y., Gordesky-Gold, B., Leney-Greene, M., Weinbren, N. L., Tudor, M. & Cherry, S. Inflammation-Induced,
263   STING-Dependent Autophagy Restricts Zika Virus Infection in the Drosophila Brain. *Cell Host Microbe* (2018)
264   **24**, 57-68 e53. PMC6173519.
265 33 Martin, M., Hiroyasu, A., Guzman, R. M., Roberts, S. A. & Goodman, A. G. Analysis of Drosophila STING
266   Reveals an Evolutionarily Conserved Antimicrobial Function. *Cell Rep* (2018) **23**, 3537-3550 e3536.
267   PMC6114933.
268 34 Cai, H., Holleufer, A., Simonsen, B., Schneider, J., Lemoine, A., Gad, H. H., Huang, J., Huang, J., Chen, D.,
269   Peng, T., Marques, J. T., Hartmann, R., Martins, N. E. & Imler, J. L. 2'3'-cGAMP triggers a STING- and NF-
270   kappaB-dependent broad antiviral response in Drosophila. *Sci Signal* (2020) **13**
271 35 Gao, P., Ascano, M., Zillinger, T., Wang, W., Dai, P., Serganov, A. A., Gaffney, B. L., Shuman, S., Jones, R.
272   A., Deng, L., Hartmann, G., Barchet, W., Tuschl, T. & Patel, D. J. Structure-function analysis of STING
273   activation by c[G(2',5')pA(3',5')p] and targeting by antiviral DMXAA. *Cell* (2013) **154**, 748-762. PMC4386733.
274 36 Holleufer, A., Winther, K. G., Gad, H. H., Ai, X., Chen, Y., Li, L., Wei, Z., Deng, H., Liu, J., Frederiksen, N. A.,
275   Simonsen, B., Andersen, L. L., Kleigrewe, K., Pichlmair, A., Cai, H., Imler, J. L. & Hartmann, R. Two cGAS-
276   like receptors induce a Sting-dependent antiviral immune response in Drosophila melanogaster. *Submitted*
277   *Manuscript* (2021)
278

314   **Author Information:** The authors have no competing financial interests to declare.

315   Correspondence and requests for materials should be addressed to P.J.K.

Figure Legends

317 **Figure 1 | Structural remodeling in animal cGLRs enables divergent pattern recognition.**

318 **a,** Crystal structures and surface electrostatic views of human MB21D2 and a cGLR from the

319 beetle *T. castaneum* (*Tc*-cGLR). Structural comparison with the human cGAS–DNA complex

320 (PDB 6CTA) reveals that cGLRs adopt a conserved overall architecture with a

321 nucleotidyltransferase signaling core and shared primary ligand-binding surface (indicated by

322 dashed lines). **b**, Zoom-in cutaways highlighting structural insertions and deletions unique to each

323 cGLR. hMB21D2 and *Tc*-cGLR lack the Zn-ribbon motif present in cGAS (left) and hMB21D2

324 contains a C-terminal α-helix extension that contacts the central "spine" helix (right). Specific

325 alterations in the predicted ligand-binding surfaces suggest individual cGLRs are remodeled for

326 recognition of different molecular patterns. **c**, Thin-layer chromatography (TLC) analysis and

327 quantification of *Tc*-cGLR enzymatic reactions in the presence of candidate 40 nt or bp nucleic

328 acid ligands. In contrast to mouse cGAS recognition of dsDNA, *Tc*-cGLR synthesizes a nucleotide

329 product specifically in response to recognition of dsRNA confirming altered ligand specificity. Data

330 are relative to maximum enzymatic activity and represent the mean ± SEM for n = 3 independent

331 experiments.

332

333 **Figure 2 | *Drosophila* cGLR1 senses long double-stranded RNA.**

334 **a,** Summary of a forward biochemical screen of 53 cGLR proteins in the order *Diptera*. cGLR

335 genes were selected based on predicted structural homology to *Tc*-cGLR and human cGAS, and

336 conservation of putative nucleotidyltransferase catalytic residues. Screened enzymes are

337 denoted with a red dot, and active dsRNA-sensors are denoted with a blue circle. The phylogeny

338 represents 153 proteins clustered into Clades 1–5, with <30% sequence identity between clades.

339 41/42 *Diptera* species are represented in Clade 5, which contains *D. melanogaster* CG12970

340 (cGLR1) and CG30424. **b,** Functional *Diptera* cGLRs identified in the biochemical screen are

341 activated to form a nucleotide product by the dsRNA mimic poly I:C. **c,** A single mutation to the

342   *Dm*-cGLR1 active site disrupts all enzymatic activity. **d,** *Dm*-cGLR1 *in vitro* activity was monitored

343   in the presence of a panel of synthetic dsRNAs from 10–40 bp and quantified relative to 40 bp

344   reactions. **e,** Electrophoretic mobility shift assay (EMSA) shows binding between *Ds*-cGLR1 and

345   a 40 bp dsRNA. Formation of a higher order protein–nucleic acid complex which does not migrate

346   through the gel is also observed with human cGAS and a 45 bp dsDNA ligand, in contrast to 2:2

347   binding between mouse cGAS and dsDNA. **f,** Model of the *Tc*-cGLR–dsRNA complex based on

348   the hcGAS–dsDNA structure (PDB 6CTA). Predicted *Dm*-cGLR1 (*Ds*-cGLR1) ligand-binding

349   residues R23 (41), K42 (60), K52 (70), R 241 (259) and K251 (269) are analogous to *Tc*-cGLR

350   residues R22, K40, R51, R249, and K259 respectively. **g,** Analysis and quantification of *in vitro*

351   *Ds*-cGLR1 activity demonstrates that charge-swap mutations to ligand-binding residues

352   significantly impair enzyme activation (see also **Extended Data Fig. 3**) **h**, Analysis of *Dm*-cGLR1

353   activity in human cells using a mammalian STING-controlled IFN-β luciferase reporter. IFN-β is

354   quantified relative to vector control and shown here relative to wild-type activity. *Dm*-cGLR1

355   signaling to STING is strictly dependent on poly I:C stimulation and mutation of the catalytic site

356   or predicted ligand-binding residues ablates this activity. Data in **h** are mean ± SEM of n = 3

357   technical replicates and representative of n = 3 independent experiments; all other data are the

358   mean ± SEM of n = 3 independent experiments.

359

360   **Figure 3 | Discovery of 3′2′-cGAMP as a metazoan nucleotide second messenger.**

361   **a,** HPLC chromatogram of the *Dm*-cGLR1 reaction (orange) and comparison with synthetic

362   nucleotide standards. *Dm*-cGLR1 synthesizes 3′2′-cGAMP as a major product that migrates

363   identical to a synthetic standard (black). The retention time of other standards are indicated with

364   a dotted line, demonstrating that a minor *Dm*-cGLR1 reaction product is 2′3′-c-di-AMP (see also

365   **Extended Data Fig. 6a**). **b,** TLC analysis of mouse cGAS and *Dm*-cGLR1 reactions labeled with

366   either α-^{32}P-ATP or α-^{32}P-GTP and treated as indicated. Schematic on right demonstrates how

367   pairwise labeling and Nuclease P1 digestion verifies that cGAS and *Dm*-cGLR1 synthesize

distinct cGAMP isomers with opposite phosphodiester linkage specificities. High-resolution mass

spectrometry confirms the major *Diptera* cGLR product as 3′2′-cGAMP (see also **Extended Data**

Fig. 6b). **c,** Inset of Clade 5 in the *Diptera* cGLR phylogeny from **Fig. 2a** annotated to denote all

enzymes identified to synthesize 3′2′-cGAMP by bacterial lysate analysis. **d,** HPLC analysis and

quantification of product formation by insect cGLRs. 3′2′-cGAMP is the dominant product of each

identified *Diptera* cGLR, and 2′3′-cGAMP is the dominant product of cGAS and *Tc*-cGLR. Data

are mean ± SEM for n = 3 independent experiments.

Figure 4 | Structural basis for 3′2′-cGAMP recognition by *Drosophila* STING

a, Thermal denaturation assay showing selective recognition of 3′2′-cGAMP *Drosophila* STING

(see also **Extended Data Fig. 8b,c**). Data shown are representative of n = 3 independent

experiments. **b**, Crystal structure of the dSTING–3′2′-cGAMP complex reveals a tightly closed

homodimer conformation and an ordered β-strand lid, indicating high-affinity engagement with the

endogenous *Drosophila* second messenger 3′2′-cGAMP. **c**, Phylogenetic alignment of the stem

helix and β-strand lid in human and insect STING proteins colored by amino-acid conservation.

Critical ligand binding residues are denoted with a navy circle and adaptations specific to *Diptera*

are highlighted in red outline. **d**, Highlight of 3′2′-cGAMP in the CDN-binding pocket of dSTING

showing key ligand contacts. **e**, Superposition of the dSTING–3′2′-cGAMP (blue-orange) and

human STING–2′3′-cGAMP (gray-pink) complexes reveals human STING readout of the 2′–5′

phosphodiester bond by the conserved R229 is absent in dSTING. dSTING R229 is stabilized in

a conformation extended outward from the ligand-binding pocket interaction with E267 on the

opposite dimer. **f**, Human STING S162 (gray) contacts the free 3′ OH of the guanosine base in

2′3′-cGAMP (pink). dSTING N159 (blue) extends across the ligand binding pocket to contact the

the free 3′ OH of the adenosine base in 3′2′-cGAMP (orange).

Figure 5 | 3′2′-cGAMP activates STING-dependent antiviral immunity in *Drosophila*.

15

394   **a,** Synthetic 3′2′-cGAMP or 3′3′-c-di-GMP was injected into the body cavity of wildtype or mutant

395   flies and gene expression measured after 24 h. *STING-regulated gene 1* (*Srg1*) RNA levels shown

396   as fold induction compared to buffer control in wildtype. dSTING$_{Mut}$ = RXN mutant, as previously

397   characterized[31,34]. Data represent RNA levels measured relative to the house-keeping gene

398   *RpL32* and are from 3 independent experiments *P ≤ 0.05; **P ≤ 0.01; ***P ≤ 0.001; and n.s., P

399   > 0.05. P value n.s. unless otherwise noted. **b,** Viral RNA loads 3 days after infection with the

400   RNA pathogen Drosophila C virus (DCV) demonstrate significantly diminished viral replication in

401   wildtype flies injected with 3′2′-cGAMP. **c,** Survival analysis of animals injected with 3′2′-cGAMP

402   or buffer control and infected with DCV. 3′2′-cGAMP injection results in a dSTING-dependent

403   response that significantly delays mortality. **d,** Survival analysis directly comparing the effects of

404   cGAMP isomers 7 days after DCV infection. cGAMP injection increases animal survival in a dose-

405   dependent manner compared to buffer control and injection of 3′2′-cGAMP confers greater

406   protection than 2′3′-cGAMP at each dose tested (see also **Extended Data Fig. 10 c,d**). **e**,

407   Proposed model for the cGLR-STING signaling. Diverse animal cGLRs recognize distinct

408   molecular patterns, respond by synthesizing a nucleotide second messenger, and induce

409   activation of STING-dependent antiviral immunity.

410 **Methods**

411 **Bioinformatics and Dipteran cGLR sequence analysis**

412 Building on previous analyses[6-12], animal cGAS homologs suitable for crystallography were

413 identified using the amino acid sequences of human cGAS and *D. melanogaster* CG7194 to seed

414 a position-specific iterative BLAST (PSI-BLAST) search of the NCBI non-redundant protein

415 database. The PSI-BLAST search was performed with an E value cutoff 0.005 for inclusion into

416 the next search round, BLOSUM62 scoring matrix, gap costs settings existence 11 and extension

417 1, and using conditional compositional score matrix adjustment. Candidate homologs identified

418 from this search included the uncharacterized human protein MB21D2 and the *Tribolium*

419 *castaneum* sequence XP_969398.1. Pairwise structural comparison between human MB21D2,

420 *Tc*-cGLR, and protein structures in the Protein Data Bank was performed using DALI[37] and Z-

421 scores for homologs less than 90% identical to one another (PDB90) were plotted in GraphPad

422 Prism. A Z-score of 15 for *Tc*-cGLR and 13 for human MB21D2 was selected as a lower cut-off

423 to emphasize direct relevant homologs in analysis.

424   Following structure determination of human MB21D2 and *T. castaneum* XP_969398.1,

425 predicted cGLRs were further identified in *Diptera* using PSI-BLAST searches seeded with either

426 *D. melanogaster* CG7194 or the *Tc*-cGLR sequence selecting in each round for proteins matching

427 known cGLR domain organization and active-site residues. *Diptera* cGLR sequences were

428 aligned using MAFFT (FFT-NS-i iterative refinement method)[38] and used to construct a

429 phylogenetic tree in Geneious Prime v2020.12.23 using the neighbor-joining method and Jukes-

430 Cantor genetic distance model with no outgroup. Further manual analysis and curation of

431 candidate cGLR sequences was performed based on alignments and predictive structural

432 homology using HHPred[39] and Phyre2[40]. Sequences were selected for predicted structural

433 homology to cGAS, including the presence of a conserved nucleotidyltransferase domain with a

434 G[S/G] activation loop and [E/D]h[E/D] X_{50-90} [E/D] catalytic triad. Manual refinement was also

435 used to exclude duplicate sequences, gene isoforms, and proteins less than 250 or greater than

436 700 residues. NCBI available genomes from 42 species in *Diptera* are represented in the final

437 tree, including 31 species in the genus *Drosophila*. Clustering of sequences in the final unrooted

438 tree was used to define clades, with no more than 30% sequence identity shared between

439 members of different clades. Further manual analysis of the tree was used to determine the

440 number and distribution of predicted cGLRs by species (see Extended Data Fig. 2a).

441 PROMALS3D[41] used for structure guided alignment of apo human cGAS (PDB 4KM5)[14],

442 hMB21D2, and *Tc*-cGLR in Extended Data Fig. 1a. MAFFT (FFT-NS-i iterative refinement

443 method)[38] was used to align STING sequences in Extended Data Fig. 8a. Geneious Prime

444 software was used to generate the sequence alignments in Figure 4 and Extended Data Figs. 1a,

445 3a and 8a.

446

447 **Protein expression and purification**

448 Recombinant cGLR and dSTING proteins were expressed and purified used methods previously

449 optimized for human cGAS[17]. Animal cGLR and dSTING sequences were codon-optimized for

450 expression in *E. coli* and cloned from synthetic constructs (GeneArt or Integrated DNA

451 Technologies) into a custom pET16 expression vector with an N-terminal 6×His-MBP fusion tag

452 or an N-terminal 6×His-SUMO2 fusion. The full-length coding sequence was used except for

453 human cGAS 157–522, mouse cGAS 147–607, human MB21D2 S29–F491, *Ds*-cGLR1 19–393,

454 and *D. eugracilis* STING 150–340 as specified. The N-terminus of *D. eugracilis* STING 150–340

455 was fused to the full-length coding sequence of T4 lysozyme connected by a Gly-Ser linker

456 sequence. Briefly, transformed BL21-CodonPlus(DE3)-RIL *E. coli* (Agilent) were grown in MDG

457 media overnight prior to inoculation of M9ZB media at an OD_{600} of 0.0475. M9ZB cultures were

458 grown to OD_{600} of 2.5 (approximately 5 h at 37°C with shaking at 230 rpm) followed by cooling on

459 ice for 20 min. Cultures were induced with 500 µM IPTG prior to incubation at 16°C overnight with

460 shaking at 230 rpm. Cultures were pelleted the following day and either flash frozen in liquid

461 nitrogen for storage at −80°C or directly lysed for purification. Selenomethionine-substituted

462   proteins for crystallography experiments were purified using a modified growth protocol as

463   previously described[30].

464   For large-scale protein purification, proteins were expressed with a 6×His-SUMO2 (Tc-

465   cGLR, *Ds*-cGLR1, *Deu*-cGLR, *Lc*-cGLR, dSTINGs) or 6×His-MBP (*Dm*-cGLR1, *Der*-cGLR1)

466   fusion tag and grown as ~4–8× 1 L cultures in M9ZB media. Pellets were lysed by sonication in

467   lysis buffer (20 mM HEPES pH 7.5, 400 mM NaCl, 30 mM imidazole, 10% glycerol and 1 mM

468   DTT) and clarified by centrifugation at ~47,850 × g for 30 min at 4°C and subsequent filtration

469   through glass wool. Recombinant protein was purified by gravity-flow over NiNTA resin (Qiagen).

470   Resin was washed with lysis buffer supplemented to 1 M NaCl and then eluted with 20 mL of lysis

471   buffer supplemented to 300 mM imidazole. SUMO2-fusion proteins were cleaved by

472   supplementing elution fractions with ~250 µg of human SENP2 protease (D364–L589 with M497A

473   mutation) during overnight dialysis at 4°C against dialysis buffer (20 mM HEPES pH 7.5, 250 mM

474   KCl, 1 mM DTT). MBP-tagged fusion proteins were buffer exchanged into lysis buffer with 4%

475   glycerol and no imidazole to optimize conditions for overnight cleavage by recombinant TEV

476   protease at ~10°C. cGLR proteins were next purified by ion exchange chromatography using

477   HiTrap Heparin HP columns (GE Healthcare) and eluted across a 150–1000 mM NaCl gradient.

478   Target protein fractions were pooled and further purified by size-exclusion chromatography using

479   a 16/600 Superdex 75 column or 16/600 Superdex 200 column and storage buffer (20 mM

480   HEPES-pH 7.5, 250 mM KCl, 1 mM TCEP). Final proteins were concentrated to ~20–30 mg mL^{-1}

481   and flash-frozen with liquid nitrogen and stored at −80°C for crystallography or supplemented with

482   10% glycerol prior to freezing for biochemistry experiments. *Tc*-cGLR and *Ds*-cGLR1 mutant

483   proteins were purified from 1 L M9ZB cultures using NiNTA affinity chromatography and overnight

484   dialysis directly into storage buffer (20 mM HEPES-pH 7.5, 250 mM KCl, 10% glycerol, 1 mM

485   TCEP) without SUMO2 tag cleavage.

486   For small-scale protein purification used in the *Diptera* cGLR screen, recombinant proteins

487   were expressed with a 6×His-MBP fusion tag with the exception of human cGAS, mouse cGAS,

488 *Tc*-cGLR, *Deu*-cGLR, *Lc*-cGLR, and *Ds*-cGLR1 which were expressed with a 6×His-SUMO2

489 fusion tag. Small-scale cultures were grown in 20 mL of M9ZB media, lysed with sonication, and

490 recombinant protein was purified as previously described[11]. Briefly, protein was purified directly

491 from lysates by centrifuge flow-through over NiNTA resin (Qiagen) in 2 mL Mini Spin columns

492 (Epoch Life Sciences). Following elution with elution buffer (20 mM HEPES pH 7.5, 400 mM NaCl,

493 300 mM imidazole, 10% glycerol and 1 mM DTT) proteins were buffer exchanged into storage

494 buffer (20 mM HEPES-pH 7.5, 250 mM KCl, 10% glycerol, 1 mM TCEP). Fresh protein

495 preparations were immediately used for *in vitro* nucleotide synthesis reactions.

496

Protein crystallization and structure determination

498 Crystals of native and selenomethionine-substituted human MB21D2 S29–F491, *Tc*-cGLR, and

499 T4 lysozyme-dSTING L150–I340, were grown at 18°C using hanging-drop vapor diffusion.

500 Optimized crystals were grown in EasyXtal 15-well trays (NeXtal Biotechnologies) with 350 μL of

501 reservoir solution and 2 μL drops set with a ratio of 1 μL protein solution and 1 μL of reservoir

502 solution. Human MB21D2 crystals were grown using a reservoir solution (1.2 M ammonium

503 sulfate, 5 mM MgCl$_2$, 100 mM MES pH 6.2) previously identified by Pei Wang and Raven Huang

504 (University of Illinois at Urbana-Champaign)[42] for 1 day prior to cryoprotection with reservoir

505 solution supplemented with 30% glycerol and freezing in liquid nitrogen. *Tc*-cGLR crystals were

506 grown using the reservoir solution (0.3 M potassium thiocyanate, 10–16% PEG-3350) for 5–16

507 days prior to cryoprotection with reservoir solution supplemented with 15% ethylene glycol and

508 freezing in liquid nitrogen. Apo T4 lysozyme-dSTING crystals were grown using the reservoir

509 solution (0.2 M sodium citrate, 0.1 M Tris-HCl, 22% PEG-3350) 7 days prior to cryoprotection with

510 reservoir solution supplemented with 15% ethylene and freezing in liquid nitrogen. T4 lysozyme-

511 dSTING–3′2′-cGAMP crystals were grown using the reservoir solution (0.1–0.2 M sodium acetate

512 pH 4.8, 0.2 M ammonium formate, 20–22% PEG-3350) supplemented with 250 μM 3′2′-cGAMP

513 (Biolog) for 10 days prior to cryoprotection with reservoir solution supplemented to 35% PEG-

514   3350 and freezing in liquid nitrogen. Growth of single MB21D2 and *Tc*-cGLR crystals was further

515   optimized with streak seeding. X-ray diffraction data were collected at the Advanced Photon

516   Source beamlines 24-ID-C and 24-ID-E and at the Advanced Light Source beamlines 5.0.1 and

517   8.2.2. Data were processed with XDS and Aimless[43] using the SSRL autoxds script (*A. Gonzales*).

518   Experimental phase information for all proteins was determined using data collected from

519   selenomethionine-substituted crystals. Anomalous sites were identified, and an initial map

520   generated with AutoSol within PHENIX[44]. Structural modeling was completed in Coot[45] and

521   refined with PHENIX. Refinement statistics are described in Supplementary Table 1, and all

522   structure figures were generated with PyMOL 2.3.0.

523

524   **Nucleotide product synthesis analysis**

525   cGLR nucleotide synthesis activity was analyzed by thin-layer chromatography as previously

526   described[11]. For the *Diptera* cGLR screen, recombinant protein preparations were incubated in

527   10 μL reactions containing 0.5 μL α-^{32}P labeled NTPs (~0.4 μCi each of ATP, CTP, GTP, and

528   UTP), 200 μM unlabeled NTPs, 10 mM $MgCl_2$, and 1 mM $MnCl_2$ in a final reaction buffer of 50

529   mM Tris-HCl pH 7.5, ~50 mM KCl, 1 mM TCEP. Reactions were additionally supplemented with

530   ~1 μg poly I:C or 5 μM ISD45 dsDNA as indicated. Reactions were incubated at 37°C overnight

531   and subsequently treated with 1 μL Quick CIP phosphatase (New England Biolabs) for 20 min at

532   37°C to remove unreacted phosphate signal. Each reaction was diluted 1:10 in 100 mM sodium

533   acetate pH 5.2 and 0.5 μL was spotted on a 20-cm × 20-cm PEI-cellulose thin-layer

534   chromatography plate. Plates were run with 1.5 M KH_2PO_4 solvent until ~2.5 cm from top of the

535   plate, dried at room-temperature, and exposed to a phosphor-screen prior to signal detection with

536   a Typhoon Trio Variable Mode Imager System (GE Healthcare). For all other nucleotide synthesis

537   reactions visualized by thin-layer chromatography, enzymes were tested at 5 μM with 5 μM

538   nucleic acid ligands and either 1 mM $MnCl_2$ or 10 mM $MgCl_2$ for insect cGLRs or cGAS

539   respectively. hMB21D2 activity was tested with 1 mM $MnCl_2$ and 10 mM $MgCl_2$ using the following

540   synthetic innate immune agonists: lipopeptide Pam3CSK4 (Invivogen), *S. aureus* lipoteichoic acid

541   (LTA-SA) (Invivogen), *S. cerevisiae* cell wall preparation (Zymosan) (Invivogen), *B. subtilis*

542   peptidoglycan (PGN-BS) (Invivogen), synthetic lipid A mimic (CRX-527) (Invivogen), *B. subtilis*

543   flagellin (FLA-BS) (Invivogen), imidazoquinoline (Imiquimod) (Invivogen), CpG oligonucleotide

544   (ODN 2006) (Invivogen), *S. aureus* 23S rRNA oligonucleotide (ORN Sa19) (Invivogen). Besides

545   *Diptera* screen reactions, samples were not diluted in sodium acetate prior to spotting on PEI-

546   cellulose TLC plates. TLC images were adjusted for contrast using FIJI[46] and quantified using

547   ImageQuant (8.2.0). Nucleotide product formation was measured according to the ratio of product

548   to total signal for each reaction. For Figs. 1c, 2d, 2g and Extended Data Figs. 3e, 4b, 5d relative

549   activity was calculated as percent conversion for each reaction relative to maximal conversion

550   observed by wildtype enzyme or in the presence of 40 bp dsRNA for insect cGLRs and 45 bp

551   dsRNA for cGAS.

552

553   **Electrophoretic mobility shift assay (EMSA)**

554   Analysis of *in vitro* protein–nucleic acid complex formation was conducted as previously

555   described[17]. Briefly, 1 µM 40-bp dsRNA or 45-bp dsDNA was incubated with *Ds*-cGLR1 or hcGAS

556   NTase-domain (D157–522) respectively at a gradient of protein concentrations as indicated in

557   each figure. Complex formation was performed with the final reaction buffer 20 mM HEPES-NaOH

558   pH 7.8, 75 mM KCl, 1 mM DTT. 20 µL reactions were incubated at 4°C for 20 min before

559   separation on a 2% agarose gel using 0.5 × TB buffer (45 mM Tris, 45 mM boric acid) as a running

560   buffer. The agarose gel was post-stained in 0.5 × TB buffer supplemented with 10 µg mL^{-1}

561   ethidium bromide with gentle shaking at 25°C for 45 min. Complex formation was visualized using

562   a ChemiDoc MP Imaging System (Bio-Rad).

563

564   ***In vitro* phase separation assays**

565   *In vitro* phase separation was performed as previously described with minor modifications[23,25].

566   Briefly, *Ds*-cGLR1 was labeled with AlexaFluor-488 (AF488) carboxylic acid (succinimidyl ester)

567   (Thermo Fisher Scientific) according to manufacturer's manuals using a molar ratio of 1:10 at 4°C

568   for 4 h. Excess free dye was removed by dialysis against buffer (20 mM HEPES-KOH pH 7.5,

569   250 mM KCl, 1 mM DTT) at 4°C overnight and AF488-labeled *Ds*-cGLR1 was then further purified

570   on a PD-10 desalting column (GE Healthcare) eluted with storage buffer (20 mM HEPES-KOH

571   pH 7.5, 250 mM KCl, 1 mM TCEP). Final AF488-labeled *Ds*-cGLR1 was concentrated to ~5 mg

572   mL^{-1}, flash-frozen in liquid nitrogen, and stored as aliquots at −80°C. hcGAS and hcGAS NTase-

573   domain (D157–F522) proteins were prepared as previously described[25].

574   To induce phase separation, *Ds*-cGLR1 (10 μM, containing 1 μM AF488-labeled *Ds*-

575   cGLR1) was mixed with various lengths of RNA (10 μM each) in buffer (20 mM Tris-HCl pH 7.5,

576   1 mg mL^{-1} BSA, 1 mM TCEP) in the presence of various salt concentrations at 25°C in a total

577   reaction volume of 20 μL. The details of proteins, nucleic acids, and salt concentrations are

578   indicated in figures. *Ds*-cGLR1–RNA reactions were placed in 384-well non-binding microplates

579   (Greiner Bio-One) and incubated at 25°C for 30 min prior to imaging to allow condensates to

580   settle. Fluorescence microscopy images were acquired at 25°C using a Leica TCS SP5 X (Leica

581   Microsystems) mounted on an inverted microscope (DMI6000; Leica Microsystems) with an oil

582   immersion 63×/numerical aperture 1.4 objective lens (HCX PL APO; Leica Microsystems).

583   AF488-labeled *Ds*-cGLR1, hcGAS and hcGAS NTase-domain proteins were detected with

584   excitation at 488 nm (emission at 500–530 nm). Microscopy images were processed with FIJI[46],

585   and contrast adjusted with a uniform threshold setup for each enzyme.

586

587   **Cellular STING signaling assays**

588   Human HEK293T cells were maintained in complete media (DMEM supplemented with penicillin,

589   streptomycin, and 10% fetal bovine serum) at 37°C. For all assays 4.5×10^4 cells were plated in

590   96-well plates. STING and cGLR activity assays were performed using Dual-Luciferase Reporter

591 Assay System (Promega) as previously described[14], with modifications. Lipofectamine-2000 was

592 used to transfect IFNβ-firefly luciferase and TK-Renilla luciferase reporters and 5 ng of pcDNA4-

593 mouse STING or 15 ng pcDNA4-dSTING. For cGLR signaling assays 150 ng of *Drosophila*

594 cGLR1, 30 ng human cGAS balanced with empty vector, or 150 ng empty vector were additionally

595 transfected. Native cGLR and STING coding sequences were expressed from a pcDNA4 vector.

596 24–30 h after transfection luciferase was measured using a GloMax microplate reader (Promega)

597 and relative IFNβ expression calculated by normalizing firefly to Renilla readings. For poly I:C

598 stimulation of cGLR activity, cells were transfected with 100 ng poly I:C (6.125–200 ng for titration

599 experiment) 5 h after plasmid transfection. For dSTING signaling assays a final concentration of

600 500 pM to 50 µM 2′3-cGAMP or 3′2′-cGAMP was delivered to cells using a digitonin

601 permeabilization buffer[47] 10 h prior to luciferase measurement.

602

603 **Nucleotide purification and HPLC analysis**

604 Enzymatic synthesis of cGLR nucleotide products for HPLC analysis was performed using 100

605 µL reactions containing 10 µM cGLR enzyme, 200 µM ATP, 200 µM GTP, 10 µg poly I:C, 1 mM

606 $MnCl_2$ and 50 mM Tris-HCl pH 7.5. Protein storage buffer (20 mM HEPES pH 7.5, 250 mM KCl,

607 1 mM TCEP) was used as necessary to adjust KCl concentration to ~100 mM. Reactions were

608 incubated at 37°C for 1 h and then nucleotide product was recovered by filtering reactions through

609 a 30-kDa cutoff concentrator (Amicon) to remove protein. Nucleotide products were separated on

610 an Agilent 1200 Infinity Series LC system using a C18 column (Zorbax Bonus-RP 4.6 × 150 mm,

611 3.5 µm) at 40°C. Products were eluted at a flow rate of 1 mL min^{-1} with a buffer of 50 mM NaH_2PO_4

612 pH 6.8 supplemented with 3% acetonitrile.

613 To purify the *Deu*-cGLR product for mass-spectrometry analysis, nucleotide synthesis

614 reaction conditions were scaled as previously described for bacterial cGAS/DncV-like

615 Nucleotidyltransferase reactions[11,48]. Briefly, a 10 mL reaction containing 528 nM *Deu*-cGLR

616 enzyme, 125 µM ATP, 125 µM GTP, ~250 µg poly I:C, 1 mM $MnCl_2$, 50 mM Tris-HCl 7.5, and ~25

617   mM KCl was incubated with gentle rotation for 36 h at 37°C follow by Quick CIP (NEB) treatment

618   for 6 h. The reaction was monitored using a 20 μL aliquot supplemented with α-^{32}P labeled NTPs

619   and to visualize product formation by thin-layer chromatography. Following incubation, the large-

620   scale reaction was filtered through a 10-kDa concentrator (Amicon) and purified by anion

621   exchange chromatography using a 1 mL Q-sepharose column washed with water and eluting with

622   a 0–2 M ammonium acetate gradient. Fractions corresponding to main product 3′2′-cGAMP were

623   differentiated from fractions corresponding to 2′3′-c-di-AMP by HPLC analysis. Product fractions

624   were further purified by size-exclusion chromatography using a Superdex 30 Increase 10/300 GL

625   with dH$_2$O as a running buffer. Peak fractions were eluted in 1 mL volumes, pooled, and

626   evaporated for storage prior to mass-spectrometry analysis.

627

628   **Nucleotide mass spectrometry analysis and 3′2′-cGAMP identification**

629   Purified nucleotide product samples were evaporated at 40°C under a gentle nitrogen stream.

630   The residual pellet was resuspended in 200 μL HPLC grade water (J.T. Baker), and 40 μL was

631   then mixed with 40 μL of water containing 50 ng mL^{-1} tenofovir as internal standard and

632   transferred to measuring vials.

633   Experiments for 3′2′-cGAMP identification were performed on an ACQUITY UPLC I-

634   Class/Vion IMS-QTOF high-resolution LC-MS system (Waters Corporation). Reverse phase

635   chromatographic separation was carried out at 30°C on a C18 column (Nucleodur Pyramid C18

636   50 x 3 mm; 3 μm Macherey Nagel, Düren, Germany) connected to a C18 security guard

637   (Phenomenex, Aschaffenburg, Germany) and a 2 μm column saver. Separation was achieved

638   using a binary gradient of water containing 10 mM ammonium acetate and 0.1% acetic acid

639   (solvent A) and methanol (solvent B). The analytes were eluted at a flow rate of 0.6 mL min^{-1}.

640   The eluting program was as follows: 0 to 4 min: 0% B, 4 to 7.3 min: 0 to 10% B. This composition

641   of 10% B was held for 1 min, then the organic content was increased to 30% within 2.7 min. The

642   column was then re-equilibrated to 0% B for 2 min. Total analysis run time was 13 min. High

643 resolution MS-Data were collected on a Vion IMS-QTOF mass spectrometer equipped with an

644 electrospray ionization source, operating in positive ionization mode. The capillary voltage was

645 set at 2.5 kV and the cone voltage at 40 V. The source temperature and desolvation gas

646 temperature was 150°C and 600°C, respectively. Analyte fragmentation was achieved using

647 argon as the collision gas. Collision energy of 10 V was used to obtain a low collision energy

648 spectrum. For high collision energy spectrum, the collision energy was ramped from 15 to 30 V.

649 Data acquisition was controlled by the UNIFI 1.9.4.0 software (Waters). For 3′2′-cGAMP

650 identification the retention times, drift times and fragment spectra of a synthetic 3′2′-cGAMP

651 standard (Biolog) were collected as a reference and compared to those of the suspected 3′2′-

652 cGAMP in the samples.

653

654 **3′2′-cGAMP quantification**

655 For quantification of 3′2′-cGAMP, chromatographic conditions were transferred to a API4000

656 mass spectrometer (Sciex) coupled to a Shimadzu HPLC-system (Shimadzu, Duisburg,

657 Germany). The analytes were ionized by means of electro spray ionization in positive mode

658 applying an ion spray voltage of 3000 V. Further ESI parameters were: curtain gas (CUR): 30 psi,

659 collision gas (CAD): 9, source temperature: 650°C, gas 1: 60 psi and gas 2: 45 psi, respectively.

660 Detection was performed in SRM mode, selecting first for the double-protonated parent ion of

661 3′2′-cGAMP and 3′3′-cGAMP (used in calibrator series). This resulted in the following mass

662 transitions: 3′2′-cGAMP and 3′3′-cGAMP: m/z 338.2 → 152 (quantifier), m/z 338.2 → 136

663 (identifier). Tenefovir served as the internal standard (m/z 288 → 176).

664 For 3′2′-cGAMP semi-quantitative quantification from lysate samples in the *Diptera* cGLR

665 screen, calibration curves were created by plotting peak area ratios of 3′3′-cGAMP as an internal

666 standard versus the nominal concentration of the calibrators. The calibration curve was calculated

667 using quadratic regression and 1/x weighing.

668

669   **Synthetic cyclic dinucleotide standards**

670   Synthetic nucleotide standards used for HPLC analysis and mass-spectrometry analysis were

671   purchased from Biolog Life Science Institute: 3′3′-cGAMP (cat no. C 117), 2′3′-cGAMP (cat no. C

672   161), 3′2′-cGAMP (cat no. C 238), 2′3′-c-di-AMP (cat no. C 187) and 2′3′-c-di-GMP (cat no. C

673   182).

674

675   **Nuclease P1 and poxin cleavage analysis**

676   Nuclease P1 cleavage analysis was performed using *Dm*-cGLR1 reactions labeled with either α-

677   ^{32}P-ATP or α-^{32}P-GTP as previously described[11,26]. Briefly, radiolabeled nucleotide products were

678   incubated with Nuclease P1 (80 mU, Sigma N8630) in 1× P1 buffer (30 mM NaOAc pH 5.3, 5 mM

679   ZnSO$_4$, 50 mM NaCl) for 30 min in the presence of Quick CIP (NEB).

680   Poxin cleavage reactions were carried out using purified insect viral AcNPV enzyme as

681   previously described[29,30]. For HPLC analysis of poxin cleavage, 100 µL reactions were performed

682   using 100 µM synthetic 2′3′-cGAMP or 3′2′-cGAMP, 50 nM AcNPV poxin, 50 mM HEPES pH 7.5,

683   10 mM KCl, and 1 mM TCEP. Reactions were incubated at 37°C and at each specified time

684   reactions were terminated by heat-inactivation at 95°C for 2 min prior to HPLC analysis as

685   described above. For thin-layer chromatography analysis of poxin cleavage, reactions were

686   performed using α-^{32}P-GTP-labeled 2′3′-cGAMP synthesized by mcGAS or 3′2′-cGAMP

687   synthesized by *Deu*-cGLR in 5 µL reactions containing 2.5 µM nucleotide product and 1 µM

688   AcNPV poxin, 50 mM HEPES pH 7.5, 10 mM KCl, and 1 mM TCEP. Reactions were incubated

689   at 37°C and at each specified time reactions were terminated by heat-inactivation at 80°C for 5

690   min prior to PEI-cellulose thin-layer chromatography analysis as described above.

691

692   **STING CDN thermal shift assay**

693   A final concentration of 15 µM dSTING was mixed with 3× SYPRO orange dye and 100 µM

694   synthetic CDN (Biolog) (or as described in figure) in 20 mM HEPES-KOH pH 7.5 and 100 mM

695 KCl. Samples were heated from 20–95°C in a BioRad CFX thermocycler with HEX channel

696 fluorescence measurements every 0.5°C. The derivative of each curve over time was calculated

697 using GraphPad Prism and graphed as a percent maximum change in fluorescence or used to

698 calculate the melting temperature.

699

700 ***D. melanogaster* cyclic dinucleotide injection and signaling analysis**

701 Fly stocks were raised on standard cornmeal agar medium at 25°C. All fly lines used in this study

702 were *Wolbachia* free. w^{1118}, *dSTING^{Control}*, and *dSTING^{Rxn}* stocks have been described

703 previously[31,34]. *Relish^{E20}* flies isogenized to the DrosDel w^{1118} isogenic background were a kind

704 gift from Luis Teixeira (Instituto Gulbenkian de Ciência)[49]. Cyclic dinucleotides including 3′2′-

705 cGAMP (Biolog), 2′3′-cGAMP (Invivogen) and 3′3′-c-di-GMP (Invivogen) were dissolved in 10 mM

706 Tris-HCl pH 7.5 and diluted to the indicated concentrations. 3–5 days old adult flies were injected

707 with 69 nL of cyclic dinucleotide solution or 10 mM Tris-HCl pH 7.5 (negative control) by

708 intrathoracic injection using a Nanoject II apparatus (Drummond Scientific). Flies were collected

709 24 h later in pools of 6 individuals (3 males and 3 females) and homogenized for RNA extraction

710 and RT-qPCR analysis, as described[34].

711

712 ***D. melanogaster* viral challenge assays**

713 For 3′2′-cGAMP and virus co-injection, flies were injected with 69 nL of virus (DCV: 5 PFU, VSV:

714 2000 PFU) in 10 mM Tris-HCl pH 7.5 or in a 0.9 mg mL^{-1} 3′2′-cGAMP solution. For titration

715 experiments comparing cGAMP isomers, 69 nL of DCV (5 pfu) in serial diluted concentrations of

716 2′3′-cGAMP or 3′2′-cGAMP were injected in the body cavity of the flies. Survival was monitored

717 daily and flies were collected in pools of 6 individuals (3 males and 3 females) at the indicated

718 time points to monitor the viral RNA load by RT-qPCR.

719

720 **Extended References**

721 3   Gao, P., Ascano, M., Wu, Y., Barchet, W., Gaffney, B. L., Zillinger, T., Serganov, A. A., Liu, Y., Jones, R. A.,
722   Hartmann, G., Tuschl, T. & Patel, D. J. Cyclic [G(2',5')pA(3',5')p] is the metazoan second messenger produced
723   by DNA-activated cyclic GMP-AMP synthase. *Cell* (2013) **153**, 1094-1107. PMC4382009.
724 6   Kranzusch, P. J. cGAS and CD-NTase enzymes: structure, mechanism, and evolution. *Curr Opin Struct Biol*
725   (2019) **59**, 178-187. PMC7127440.
726 7   Wu, J. & Chen, Z. J. Innate immune sensing and signaling of cytosolic nucleic acids. *Annu Rev Immunol*
727   (2014) **32**, 461-488
728 8   Burroughs, A. M., Zhang, D., Schaffer, D. E., Iyer, L. M. & Aravind, L. Comparative genomic analyses reveal
729   a vast, novel network of nucleotide-centric systems in biological conflicts, immunity and signaling. *Nucleic*
730   *Acids Res* (2015) **43**, 10633-10654. PMC4678834.
731 9   Wu, X., Wu, F. H., Wang, X., Wang, L., Siedow, J. N., Zhang, W. & Pei, Z. M. Molecular evolutionary and
732   structural analysis of the cytosolic DNA sensor cGAS and STING. *Nucleic Acids Res* (2014) **42**, 8243-8257.
733   PMC4117786.
734 10   Kranzusch, P. J., Wilson, S. C., Lee, A. S., Berger, J. M., Doudna, J. A. & Vance, R. E. Ancient Origin of
735   cGAS-STING Reveals Mechanism of Universal 2',3' cGAMP Signaling. *Mol Cell* (2015) **59**, 891-903.
736   PMC4575873.
737 11   Whiteley, A. T., Eaglesham, J. B., de Oliveira Mann, C. C., Morehouse, B. R., Lowey, B., Nieminen, E. A.,
738   Danilchanka, O., King, D. S., Lee, A. S. Y., Mekalanos, J. J. & Kranzusch, P. J. Bacterial cGAS-like enzymes
739   synthesize diverse nucleotide signals. *Nature* (2019) **567**, 194-199. PMC6544370.
740 12   de Oliveira Mann, C. C., Kiefersauer, R., Witte, G. & Hopfner, K. P. Structural and biochemical characterization
741   of the cell fate determining nucleotidyltransferase fold protein MAB21L1. *Sci Rep* (2016) **6**, 27498.
742   PMC4897736.
743 13   Civril, F., Deimling, T., de Oliveira Mann, C. C., Ablasser, A., Moldt, M., Witte, G., Hornung, V. & Hopfner, K.
744   P. Structural mechanism of cytosolic DNA sensing by cGAS. *Nature* (2013) **498**, 332-337. PMC3768140.
745 14   Kranzusch, P. J., Lee, A. S., Berger, J. M. & Doudna, J. A. Structure of human cGAS reveals a conserved
746   family of second-messenger enzymes in innate immunity. *Cell Rep* (2013) **3**, 1362-1368. PMC3800681.
747 17   Zhou, W., Whiteley, A. T., de Oliveira Mann, C. C., Morehouse, B. R., Nowak, R. P., Fischer, E. S., Gray, N.
748   S., Mekalanos, J. J. & Kranzusch, P. J. Structure of the Human cGAS-DNA Complex Reveals Enhanced
749   Control of Immune Surveillance. *Cell* (2018) **174**, 300-311 e311. PMC6084792.
750 23   Du, M. & Chen, Z. J. DNA-induced liquid phase condensation of cGAS activates innate immune signaling.
751   *Science* (2018) **361**, 704-709
752 25   Zhou, W., Mohr, L., Maciejowski, J. & Kranzusch, P. J. cGAS phase separation inhibits TREX1-mediated DNA
753   degradation and enhances cytosolic DNA sensing. *Mol Cell* (2021) **81**, DOI 10.1016/j.molcel.2021.1001.1024.
754 26   Kranzusch, P. J., Lee, A. S. Y., Wilson, S. C., Solovykh, M. S., Vance, R. E., Berger, J. M. & Doudna, J. A.
755   Structure-guided reprogramming of human cGAS dinucleotide linkage specificity. *Cell* (2014) **158**, 1011-1021.
756   PMC4157622.
757 28   Morehouse, B. R., Govande, A. A., Millman, A., Keszei, A. F. A., Lowey, B., Ofir, G., Shao, S., Sorek, R. &
758   Kranzusch, P. J. STING cyclic dinucleotide sensing originated in bacteria. *Nature* (2020) **586**, 429-433.
759   PMC7572726.
760 29   Eaglesham, J. B., Pan, Y., Kupper, T. S. & Kranzusch, P. J. Viral and metazoan poxins are cGAMP-specific
761   nucleases that restrict cGAS-STING signalling. *Nature* (2019) **566**, 259-263. PMC6640140.
762 30   Eaglesham, J. B., McCarty, K. L. & Kranzusch, P. J. Structures of diverse poxin cGAMP nucleases reveal a
763   widespread role for cGAS-STING evasion in host-pathogen conflict. *Elife* (2020) **9**. PMC7688311.
764 31   Goto, A., Okado, K., Martins, N., Cai, H., Barbier, V., Lamiable, O., Troxler, L., Santiago, E., Kuhn, L., Paik,
765   D., Silverman, N., Holleufer, A., Hartmann, R., Liu, J., Peng, T., Hoffmann, J. A., Meignin, C., Daeffler, L. &
766   Imler, J. L. The Kinase IKKbeta Regulates a STING- and NF-kappaB-Dependent Antiviral Response Pathway
767   in Drosophila. *Immunity* (2018) **49**, 225-234 e224. PMC6267954.
768 34   Cai, H., Holleufer, A., Simonsen, B., Schneider, J., Lemoine, A., Gad, H. H., Huang, J., Huang, J., Chen, D.,
769   Peng, T., Marques, J. T., Hartmann, R., Martins, N. E. & Imler, J. L. 2'3'-cGAMP triggers a STING- and NF-
770   kappaB-dependent broad antiviral response in Drosophila. *Sci Signal* (2020) **13**
771 37   Holm, L. DALI and the persistence of protein shape. *Protein Sci* (2020) **29**, 128-140. PMC6933842.
772 38   Katoh, K. & Standley, D. M. MAFFT multiple sequence alignment software version 7: improvements in
773   performance and usability. *Mol Biol Evol* (2013) **30**, 772-780. PMC3603318.
774 39   Gabler, F., Nam, S. Z., Till, S., Mirdita, M., Steinegger, M., Soding, J., Lupas, A. N. & Alva, V. Protein Sequence
775   Analysis Using the MPI Bioinformatics Toolkit. *Curr Protoc Bioinformatics* (2020) **72**, e108
776 40   Kelley, L. A., Mezulis, S., Yates, C. M., Wass, M. N. & Sternberg, M. J. The Phyre2 web portal for protein
777   modeling, prediction and analysis. *Nat Protoc* (2015) **10**, 845-858. PMC5298202.
778 41   Pei, J. & Grishin, N. V. PROMALS3D: multiple protein sequence alignment enhanced with evolutionary and
779   three-dimensional structural information. *Methods Mol Biol* (2014) **1079**, 263-271. PMC4506754.
780 42   Wang, P. Discovery and characterization of novel RNA repair systems. (2015),
781   http://hdl.handle.net/2142/78582
782 43   Kabsch, W. Xds. *Acta Crystallogr D Biol Crystallogr* (2010) **66**, 125-132. PMC2815665.

783	44	Liebschner, D. *et al.* Macromolecular structure determination using X-rays, neutrons and electrons: recent
784		developments in Phenix. *Acta Crystallogr D Struct Biol* (2019) **75**, 861-877. PMC6778852.
785	45	Emsley, P. & Cowtan, K. Coot: model-building tools for molecular graphics. *Acta Crystallogr D Biol Crystallogr*
786		(2004) **60**, 2126-2132
787	46	Schindelin, J., Arganda-Carreras, I., Frise, E., Kaynig, V., Longair, M., Pietzsch, T., Preibisch, S., Rueden, C.,
788		Saalfeld, S., Schmid, B., Tinevez, J. Y., White, D. J., Hartenstein, V., Eliceiri, K., Tomancak, P. & Cardona, A.
789		Fiji: an open-source platform for biological-image analysis. *Nat Methods* (2012) **9**, 676-682. PMC3855844.
790	47	Woodward, J. J., Iavarone, A. T. & Portnoy, D. A. c-di-AMP secreted by intracellular Listeria monocytogenes
791		activates a host type I interferon response. *Science* (2010) **328**, 1703-1705. PMC3156580.
792	48	Lowey, B., Whiteley, A. T., Keszei, A. F. A., Morehouse, B. R., Mathews, I. T., Antine, S. P., Cabrera, V. J.,
793		Kashin, D., Niemann, P., Jain, M., Schwede, F., Mekalanos, J. J., Shao, S., Lee, A. S. Y. & Kranzusch, P. J.
794		CBASS Immunity Uses CARF-Related Effectors to Sense 3'-5'- and 2'-5'-Linked Cyclic Oligonucleotide
795		Signals and Protect Bacteria from Phage Infection. *Cell* (2020) **182**, 38-49 e17. PMC7728545.
796	49	Ferreira, A. G., Naylor, H., Esteves, S. S., Pais, I. S., Martins, N. E. & Teixeira, L. The Toll-Dorsal Pathway Is
797		Required for Resistance to Viral Oral Infection in Drosophila. *PLoS pathogens* (2014) **10**
798	50	Cohen, D., Melamed, S., Millman, A., Shulman, G., Oppenheimer-Shaanan, Y., Kacen, A., Doron, S., Amitai,
799		G. & Sorek, R. Cyclic GMP-AMP signalling protects bacteria against viral infection. *Nature* (2019) **574**, 691-
800		695
801	51	Zhao, Z., Ma, Z., Wang, B., Guan, Y., Su, X. D. & Jiang, Z. Mn(2+) Directly Activates cGAS and Structural
802		Analysis Suggests Mn(2+) Induces a Noncanonical Catalytic Synthesis of 2'3'-cGAMP. *Cell Rep* (2020) **32**,
803		108053
804		

805   **Data Availability Statement:** Coordinates and structure factors of human MB21D2, *T.*

806   *castaneum* cGLR, *Drosophila* STING, and the *Drosophila* STING–3′2′-cGAMP complex have

807   been deposited in PDB under the accession codes 7LT1, 7LT2, 7MWY, and 7MWZ. All other data

808   are available in the manuscript or the supplementary materials.

809

810   **Extended Data Figure Legends**

811   **Extended Data Figure 1 | Sequence and structural analysis of hMB21D2 and *Tc*-cGLR.**

812   **a,** Structure guided sequence alignment of the catalytic domain of human cGAS (PDB 4KM5),

813   human MB21D2, and *Tc*-cGLR. Strict secondary structure conservation further supports

814   conserved structural homology despite primary sequence divergence. The [D/E]hD[X$_{50-90}$]D

815   catalytic triad is highlighted with red outline and the human Zn-ribbon insertion that is absent in

816   other cGLRs is denoted with magenta line. hMB21D2 contains an additional 61 residues which

817   are not resolved in the crystal structure and are absent from the alignment. **b,c,** Zoom-in cutaways

818   of the human MB21D2 and *Tc*-cGLR crystal structures highlighting positioning of conserved

819   catalytic residues in the nucleotidyltransferase active site. In human cGAS the analogous residues

820   coordinate two Mg^{2+} metal ions to control synthesis of 2′3′-cGAMP (inset, middle; PDB 6CTA).

821 The hMB21D2 structure is in an inactive state distinguished by misaligned catalytic residues and

822 occlusion by an extended Gly-Gly-activation loop, indicating that catalytic activation is likely

823 controlled by a conformational rearrangement. **d, e,** TLC analysis of *in vitro* tests for potential

824 activating ligands of hMB21D2. No nucleotide products were identified upon stimulation with 40

825 nt or bp nucleic acid ligands (**d**) or ligands known to activate mammalian Toll-like receptors (**e**) **f,**

826 Z-score structural similarity plot showing homology between human MB21D2 and *Tc*-cGLR with

827 representative structures in the Protein Data Bank (PDB90). Increasing Z-score indicates greater

828 homology confirming the close relationship between animal cGLR enzymes and more distantly

829 related similarity with cGAS/DncV-like Nucleotidyltransferases (CD-NTases) in bacterial anti-

830 phage defense systems[11,50]. Z-scores cutoffs are 13 and 15 for hMB21D2 and *Tc*-cGLR

831 respectively.

832

833 **Extended Data Figure 2 | Forward biochemical screen of predicted cGLRs in Diptera.**

834 **a,** Violin plot showing the number of predicted cGLRs in *Diptera* genomes. *Drosophila* genomes

835 (n = 31 species) have a median of four predicted cGLRs in contrast to a median of two predicted

836 cGLRs in other Dipteran insects (n = 11 species). **b,** Schematic of *in vitro* screen of predicted

837 cGLRs in the order *Diptera*. 53 sequences were selected representing each clade in the

838 phylogeny in **Fig. 2a**. Following recombinant protein expression in *E. coli*, lysates were split into

839 two samples for parallel TLC analysis of *in vitro* enzymatic activity and HPLC-MS analysis of

840 lysate nucleotide metabolites. **c, d,** Purified cGLR proteins were incubated overnight at 37°C with

841 α^{32}P-radiolabeled nucleotides, a mixture of Mn^{2+} and Mg^{2+}, and the 45 bp immunostimulatory DNA

842 ISD45 or the synthetic dsRNA analog poly (I:C) as potential nucleic acid ligands, and reactions

843 were visualized by PEI-cellulose TLC. Wild-type and catalytically inactive mouse cGAS enzymes

844 were used as controls for each sample set. Note that mouse cGAS exhibits dsDNA-independent

845 activity in the presence of Mn^{2+}[51]. Predicted *Diptera* cGLRs grouped by clade (DC01–05) and

846 numbered within each clade. Ligand-dependent activity was identified for DC02_01, 05_03,

847   05_19, and 05_21; species listed below. We observed ligand-independent activity for two

848   enzymes in Clade 3. Data represent n = 2 independent experiments. **e,** SDS-PAGE and

849   Coomassie stain analysis of NiNTA purified cGLR protein fractions used for the biochemical

850   screen. **f,** SDS-PAGE and Coomassie stain analysis of final NiNTA, ion-exchange, and size-

851   exclusion purified cGLR proteins used for biochemical studies.

852

853   **Extended Data Figure 3 | Sequence analysis and mutagenesis of insect cGLRs.**

854   **a,** Alignment of the catalytic domain of human cGAS and active cGLRs identified in *T. castaneum*,

855   *D. eugracilis*, *L. cuprina*, *D. erecta*, *D. simulans*, and *D. melanogaster*. The EhD[X$_{50-90}$]D catalytic

856   triad is highlighted with red outline and the human Zn-ribbon insertion that is absent in insect

857   cGLRs is denoted with a dashed red outline. cGLRs from *D. erecta* and *D. simulans* are close

858   homologs of *Dm*-cGLR1 (76% and 91% sequence identity, respectively) and thus are also

859   referred to as "cGLR1". All biochemical experiments with *Ds*-cGLR1 were performed with a

860   construct beginning at M19. **b–c,** *In vitro* nucleotide synthesis reactions demonstrating effect of

861   mutations to catalytic residues (**b**) or putative ligand binding groove (**c**) on insect cGLR enzymatic

862   activity. Catalytic active-site mutations ablate nucleotide product synthesis and ligand-binding

863   groove mutations that disrupt predicted RNA contacting residues significantly impair product

864   synthesis. **d,** SDS-PAGE and Coomassie stain analysis of purified wild-type and mutant proteins,

865   as labeled in above TLC images. **e,** *Above*, structure of *Tc*-cGLR1 modeled with dsRNA as shown

866   in **Fig. 2f**, indicating putative ligand binding residues in *Tc*-cGLR selected analysis. *Below*,

867   quantification of *in vitro* activity of *Tc*-cGLR in **c**, as displayed in **Fig. 2g** for *Ds*-cGLR1. Data are

868   mean ± SEM, quantified relative to wild-type activity and represent n = 3 independent

869   experiments. **f,** IFN-β luciferase assay in which cGLRs are expressed in human cells and CDN-

870   synthesis is detected by mammalian STING activation. IFN-β quantified relative to empty vector

871   control. In comparison to human cGAS control which is activated by expression vector-plasmid

872   DNA, *Dm*-cGLR1 (left) and *Ds*-cGLR1 (right) require poly I:C stimulation to activate a downstream

873 STING response. Mutation to catalytic residues or putative ligand binding residues (as indicated

874 in **Fig. 2f**) ablates cGLR activity. See also **Fig. 2h**. Data are mean ± SEM of n = 3 technical

875 replicates and representative of n = 3 independent experiments. *P ≤ 0.05; **P ≤ 0.01; ***P ≤

876 0.001; and n.s., P > 0.05. P value n.s. unless otherwise noted.

877

878 **Extended Data Figure 4 | Analysis of RNA-recognition by insect cGLRs.**

879 **a–c,** *In vitro* activity assays for each active insect cGLR demonstrating dsRNA recognition is

880 required for enzyme activation. Reactions were performed with synthetic 40 nt or bp ligands.

881 Weak *Deu*-cGLR ssRNA-stimulated activity may be explained by transient short duplex formation

882 similar to observations that some ssDNA oligos can stimulate mouse cGAS dsDNA-dependent

883 activity[3]. **b,** TLC and quantification for enzyme activation in the presence of a panel of 10–40 bp

884 synthetic dsRNA ligands. 30 bp dsRNA is sufficient to stimulate maximal activity for *Tc*-, *Dm*-, and

885 *Lc*- cGLRs, while *Ds*-cGLR1 requires 35 bp and *Deu*-cGLR can be activated by dsRNAs as short

886 as 15 bp. **c,** Reactions with 146 bp *in vitro* transcribed dsRNAs either retaining a 5′ triphosphate

887 or 5′ OH termini demonstrate that dsRNA-recognition by insect cGLRs does not involve 5′ end

888 discrimination. Data are mean ± SEM, quantified relative to maximum observed activity and

889 represent n = 3 independent experiments. **d,** Deconvolution of catalytic metal requirements for

890 enzymatic activity by insect cGLRs. Insect cGLRs require Mn^{2+} for maximal catalytic activity with

891 weak product formation observed in the presence of Mg^{2+}. Data represent n = 3 independent

892 experiments. **e,** Poly I:C titration demonstrates dsRNA-stimulation of *Drosophila* cGLR1 activity

893 in cells is dependent on RNA concentration. IFN-β luciferase assay in which cGLRs are expressed

894 in human cells and CDN-synthesis is measured by mammalian STING activation, as in **Fig. 2h**

895 and **Extended Data Fig. 3f**. IFN-β quantified relative to empty vector control. Data are mean ±

896 SEM of n = 3 technical replicates and representative of n = 3 independent experiments.

897

898 **Extended Data Figure 5 | Characterization of *Ds*-cGLR1–dsRNA condensate formation.**

899   **a,** Electrophoretic mobility shift assay (EMSA) showing binding between *Ds*-cGLR1 or the C-

900   terminal nucleotidyltransferase domain of human cGAS (hcGAS-NTase) and a 40 bp dsRNA or

901   45 bp dsDNA. *Ds*-cGLR1 preferentially binds dsRNA and more weakly interacts with dsDNA,

902   consistent with observed binding between human cGAS and dsRNA[13]. **b–c,** Analysis of *Ds*-

903   cGLR1 and human cGAS (hcGAS) phase separation with AF488-labeled protein. Mammalian

904   cGAS contains a highly disordered N-terminal extension of ~150 residues, but this unstructured

905   extension is absent in insect cGLR sequences. In the presence of dsDNA, full-length hcGAS

906   forms highly dynamic liquid droplets, whereas the minimal hcGAS NTase-domain forms rigid

907   protein–DNA condensates similar to those formed by *Ds*-cGLR1–RNA complexes. Human cGAS

908   exhibits a preference for condensate formation in the presence of dsDNA while *Ds*-cGLR1

909   exhibits a preference for dsRNA (scale bar = 10 µm) (see also **Fig. 2e**). **c,** Analysis of *Ds*-cGLR1

910   dsRNA length-specificity for condensate formation demonstrates clear length-dependency and

911   supports that long dsRNA and condensate formation are required for maximal *Ds*-cGLR1

912   activation. **d,** Analysis of the impact of AF488-labeling on *Ds*-cGLR1 enzymatic activity. Similar

913   to previous observations with hcGAS[25], AF488-labeling negatively impacts enzymatic activity but

914   has minimal effect at the ratio of 90% unlabeled and 10% labeled protein used for all imaging

915   experiments. Data represent n = 3 independent experiments, and are quantified in **c** as the mean

916   ± SEM.

917

918   **Extended Data Figure 6 | Synthesis of 3′2′-cGAMP by *Diptera* cGLRs.**

919   **a,** HPLC analysis of the nucleotide products of *Tc*-cGLR, *Dm*-cGLR1, *Ds*-cGLR1, *Lc*-cGLR, and

920   *Deu*-cGLR reactions compared to relevant synthetic controls. Integration of major and minor

921   product peaks in n = 3 independent experiments were used to calculate relative product ratios

922   shown in **Fig. 3d**. **b,** The *Drosophila* cGLR major reaction product was purified from *Deu*-cGLR

923   reactions and compared to synthetic 3′2′-cGAMP with tandem mass-spectrometry analysis.

924   Parent mass extracted ion trace (left) and tandem mass spectra comparison (right) validate the

925   chemical identity of the *Drosophila* cGLR product as 3′2′-cGAMP. **c,** Heat map showing the

926   relative concentrations of cGAMP isomers detected by HPLC-MS in bacterial lysates expressing

927   *Diptera* cGLRs (as described in **Extended Data Fig. 2b**). In all cases 3′2′-cGAMP was present

928   as the dominant product with trace amounts of 3′3′- and 2′3′-cGAMP detected in some samples

929   as minor species.

930

931   **Extended Data Figure 7 | Mechanism of 3′2′-cGAMP bond formation and resistance to**

932   **degradation by viral poxin enzymes.**

933   **a,** Analysis of *Dm*-cGLR1 reactions with pairwise combinations of α-^{32}P-labeled nucleotides and

934   non-hydrolyzable nucleotides reveals reaction intermediates and identifies the order of bond

935   formation during 3′2′-cGAMP synthesis. *Left*, TLC analysis demonstrates *Dm*-cGLR1 forms a

936   linear intermediate in the presence of GTP and non-hydrolyzable ATP (Apcpp) indicating the 2′–

937   5′ phosphodiester bond is synthesized first. Exposed γ-phosphates removed by phosphatase

938   treatment prior to analysis indicated by parentheses. Note that while a linear intermediate cannot

939   be formed in the presence of non-hydrolyzable GTP (Gpcpp), *Dm*-cGLR1 will synthesize the off-

940   product 2′3′-c-di-AMP. Mouse cGAS, which synthesizes 2′3′-cGAMP through the linear

941   intermediate pppG[2′–5′]pA, is shown here for comparison[26]. *Right*, Schematic of the reaction

942   mechanism for each enzyme. Data are representative of n = 3 independent experiments. **b,**

943   Poxins are 2′3′-cGAMP-specific viral nucleases that disrupt cGAS-STING signaling. HPLC

944   analysis of synthetic 2′3′-cGAMP or 3′2′-cGAMP treated with poxin from the insect baculovirus

945   *Autographa californica* nucleopolyhedrovirus (AcNPV)[29,30]. In 1 min, AcNPV poxin cleaves 2′3′-

946   cGAMP into a mixture of intermediate and full cleavage product; and after 1 h turnover is

947   complete. No cleavage of 3′2′-cGAMP is observed by AcNPV poxin under these reaction

948   conditions. **c,** Using TLC as a more sensitive assay, we observed minimal cleavage of 3′2′-

949   cGAMP following overnight incubation with AcNPV poxin. **d,** Schematic highlighting how an

950   isomeric switch in phosphodiester linkage specificity makes 3′2′-cGAMP remarkably resistant to

951   poxin-mediated cleavage.

952

953   **Extended Data Figure 8 | Structural and biochemical analysis of *Drosophila* STING**

954   **a,** Alignment of the C-terminal cyclic dinucleotide (CDN)-binding domains of human STING,

955   mouse STING, *D. eugracilis* STING and *D. melanogaster* STING. Architecture of the core CDN-

956   binding domain is conserved across metazoans; the disordered C-terminal tail which controls

957   IRF3-IFNβ signaling is specific to vertebrates[10,28]. Ligand-interacting residues selected for

958   mutational analysis annotated with a navy circle; *Diptera*-specific adaptations highlighted with red

959   outline. All structural and biochemical experiments were performed with a *D. eugracilis* STING

960   construct ending at I340. **b,** *In vitro* thermal denaturation assay analyzing dSTING interactions

961   with a panel of CDNs. Only 3′2′-cGAMP forms a thermo-stable complex with dSTING (see also

962   **Fig. 4a**). Data are mean ± SEM of the average T_m calculated from technical duplicates in n = 3

963   independent experiments. **c,** *In vitro* thermal denaturation assay demonstrating concentration-

964   dependent thermal shift induced by 3′2′-cGAMP. **d,** Dose titration of 2′3′-cGAMP and 3′2′-cGAMP

965   in human cells demonstrating selective response by dSTING to 3′2′-cGAMP. *D. eugracilis* CDN

966   binding domain (CBD) was adapted for downstream signaling in human cells by addition of N-

967   terminal human transmembrane (hTM) domains and human C-terminal tail (hCTT). **e**,

968   Comparison of the human STING–2′3′-cGAMP and dSTING–3′2′-cGAMP crystal structures

969   reveals a conserved closed homodimer architecture in which apical "wings" are spread 32–36 Å,

970   demonstrating high-affinity engagement with an endogenous ligand. **f**, Enlarged cutaway of 3′2′-

971   cGAMP in the dSTING crystal structure, shown as simulated annealing F_O−F_C omit map. **g**, Full

972   crystal structure used to determine structure of *D. eugracilis* STING in complex with 3′2′-cGAMP.

973   T4-lysozyme is fused to the N-terminus of the *D. eugracilis* STING CDN binding domain. **h**,

974   Thermal denaturation assay as in **Fig. 4a** demonstrating that N-terminal fusion of T4 lysozyme

975   does not impair dSTING recognition of 3′2′-cGAMP. **i**, Mutational analysis of key ligand-interacting

976   residues in dSTING; thermal denaturation assay used to analyze 3′2′-cGAMP recognition.

977   Mutations which conserve functional contacts with 3′2′-cGAMP (Y164F) maintain ligand

978   recognition; mutations which ablate contacts abrogate ligand binding. N159S exhibits diminished

979   ability to recognize 3′2′-cGAMP. Data in **b** and **i** are mean ± SEM of the average T_m calculated

980   from n=2 technical replicates in n = 3 independent experiments. Data in **c** are representative of n

981   = 3 independent experiments. Data in **d** are mean ± SEM of n = 3 technical replicates and

982   representative of n = 3 independent experiments. **j,** SDS-PAGE and Coomassie stain analysis of

983   purified wild-type and mutant proteins.

984

985   **Extended Data Figure 9 | 3′2′-cGAMP induces the expression of dSTING-regulated genes.**

986   **a–d,** Injection of 3′2′-cGAMP into *D. melanogaster* has a dose-dependent effect on the expression

987   of dSTING-regulated genes. 2′3′-cGAMP was used as positive control as previously

988   characterized[31,34]. Synthetic nucleotide was injected into the body cavity of wildtype (*w^1118*) flies

989   and gene expression was measured after 24 h. RNA levels were measured relative to the house-

990   keeping gene *RpL32*, and nucleotide concentrations are displayed in µg µL^{-1}. Note that for *srg2*

991   measurement after injection of 9E-7 µg µL^{-1} 3′2′-cGAMP there was one outlier replicate with a

992   value of 0.5977 (data not shown, included in mean analysis). **e–k,** As in **Fig. 5a**, RNA expression

993   analysis of STING-regulated genes 24 h after injection with synthetic 3′2′-cGAMP or 3′3′-c-di-

994   GMP. RNA levels are shown as fold induction compared to buffer control in wildtype, *dSTING*, or

995   *Relish* mutant flies respectively. dSTING$_{Mut}$ = RXN mutant; Relish$_{Mut}$ = Relish^{E20} mutant, as

996   previously characterized[31,34]. All data represent the mean ± SEM of n = 3 independent

997   experiments, and each point represents a pool of 6 flies *P ≤ 0.05; **P ≤ 0.01; ***P ≤ 0.001; and

998   n.s., P > 0.05. P value n.s. unless otherwise noted.

999

1000   **Extended Data Figure 10 | 3′2′-cGAMP functions as a potent antiviral ligand**

1001   **a,** Analysis of Drosophila C virus (DCV) viral RNA load in flies injected with 3′2′-cGAMP or buffer

1002   control. *dSTING* wildtype and mutant flies were injected with 3′2′-cGAMP or buffer control and

1003   then infected with DCV. Viral RNA levels were measured at each time as indicated relative to the

1004   house-keeping gene *RpL32.* DCV is a picornavirus-like (+)ssRNA virus in the family

1005   *Dicistroviridae*. **b,** Analysis of vesicular stomatitis virus (VSV) viral RNA load in flies injected with

1006   3′2′-cGAMP or buffer control. *dSTING* wildtype and mutant flies were injected with 3′2′-cGAMP or

1007   buffer control as in **a** and then infected with VSV. Viral RNA levels were measured 4 days post

1008   infection relative to the house-keeping gene *RpL32.* VSV is a (-)ssRNA virus in the *Rhabdoviridae*

1009   family. **c,** (As in **a**) Analysis of Drosophila C virus (DCV) viral RNA load in flies injected with 3′2′-

1010   cGAMP, 2′3′-cGAMP, or buffer control. Viral RNA levels were measured one, two, or three days

1011   post-infection (dpi) relative to house-keeping gene *RpL32.* **d,** Survival curves after DCV infection

1012   showing effect of injection with dose titration of 3′2′-cGAMP or 2′3′-cGAMP compared to buffer

1013   control. Both cGAMP isomers significantly delay mortality in a dose-dependent manner; 3′2′-

1014   cGAMP provides greater protection in comparison to 2′3′-cGAMP. All data represent the mean ±

1015   SEM of n = 3 independent experiments, and each point represents a pool of 6 flies (**a**, **b**) or 10

1016   flies (**c, d**). *P ≤ 0.05; **P ≤ 0.01; ***P ≤ 0.001; and n.s., P > 0.05. P value n.s. unless otherwise

1017   noted.

1018

1019   **Supplementary Table 1 | Summary of X-ray crystallography data collection, phasing and**

1020   **refinement statistics.**

1021

1022   **Supplementary Table 2 | cGLR sequence information.**

Fig. 1 | Structural remodeling in animal cGLRs enables divergent pattern recognition
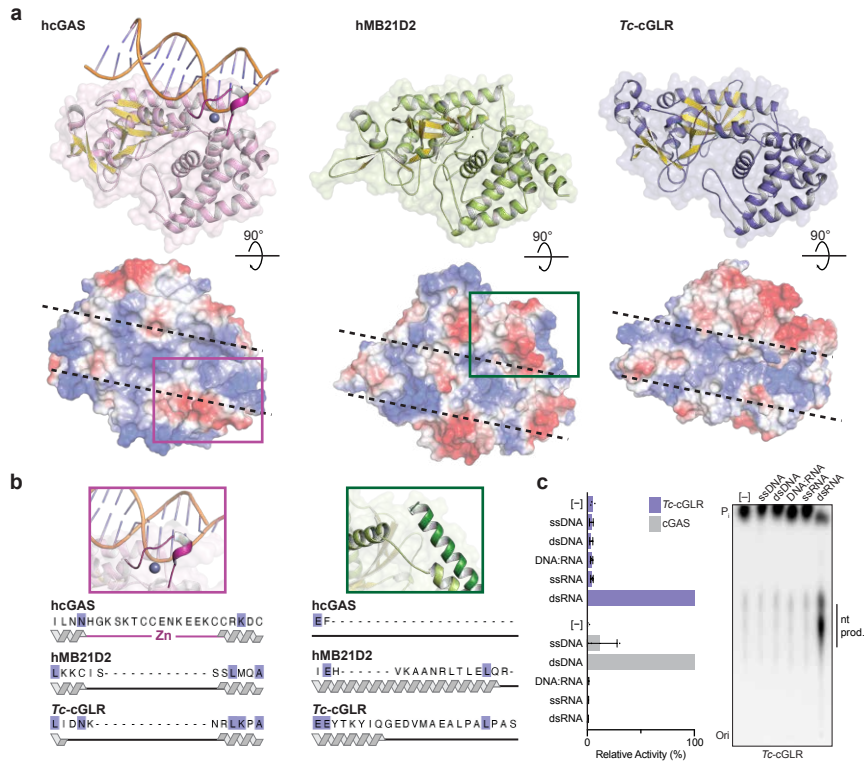
Fig. 2 | *Drosophila* cGLR1 senses long double-stranded RNA
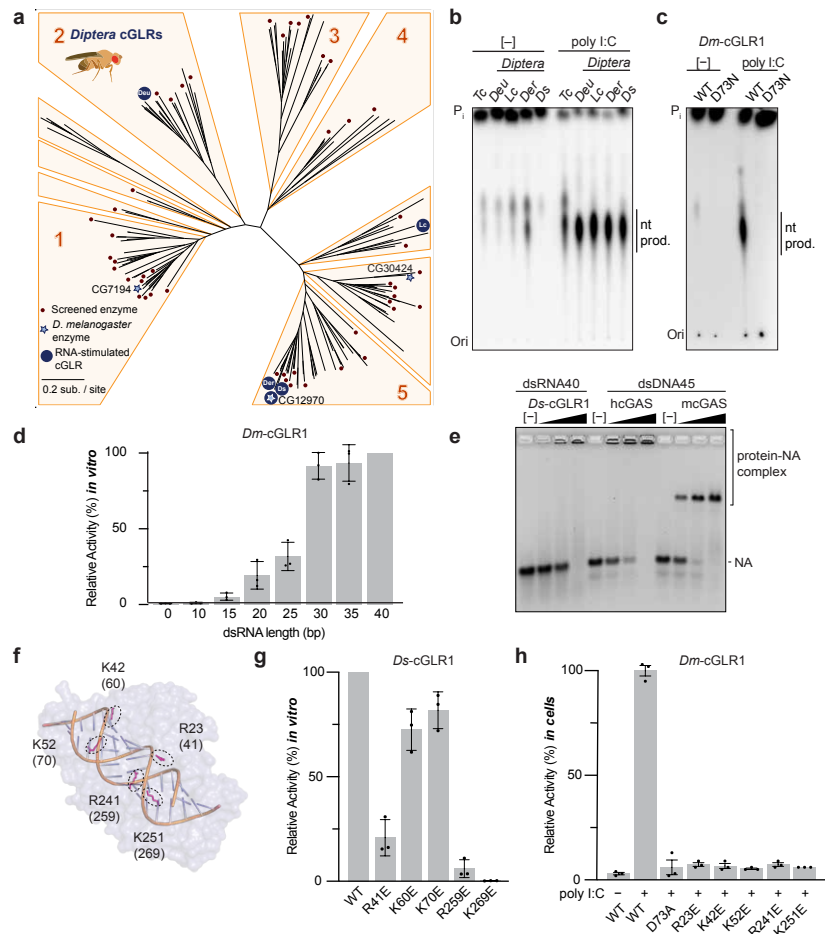
Fig. 3 | Discovery of 3′2′-cGAMP as a metazoan nucleotide second messenger
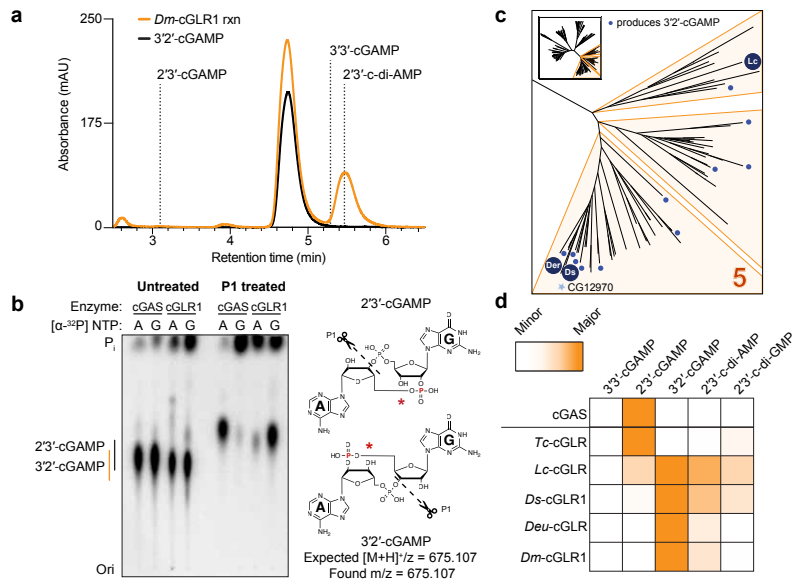
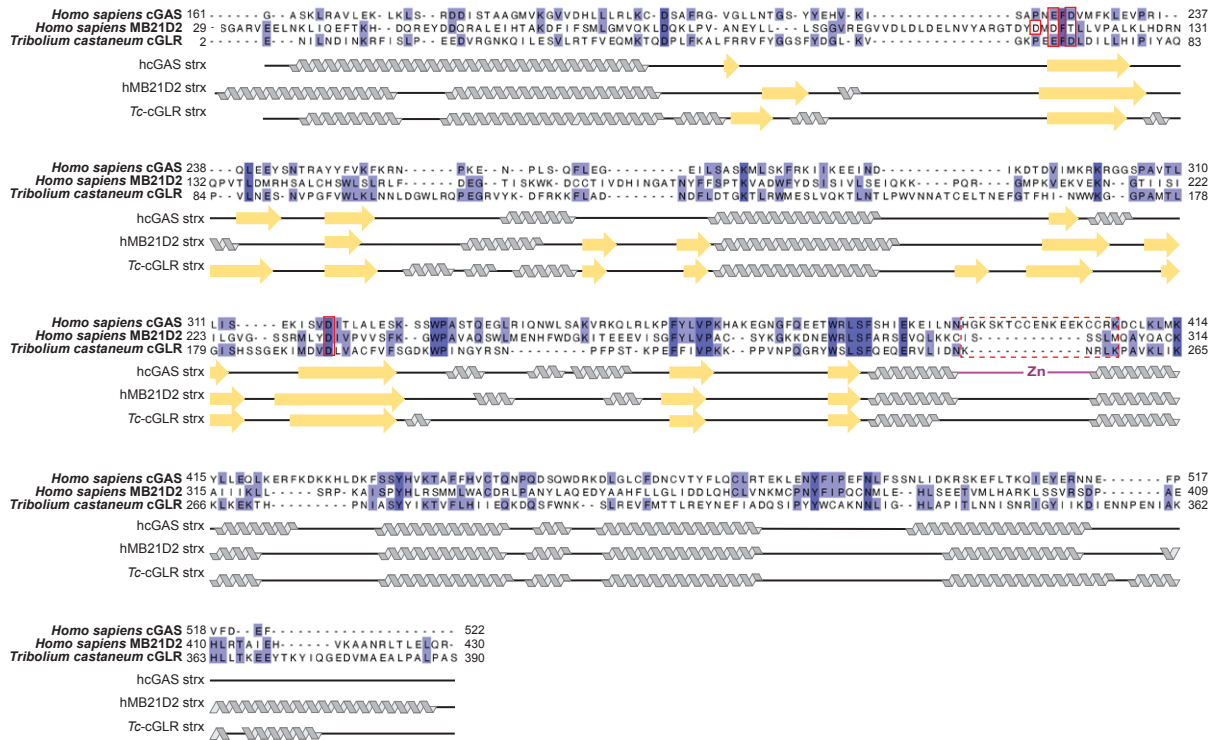**Fig. 4 | Structural basis for 3'2'-cGAMP recognition by *Drosophila* STING**
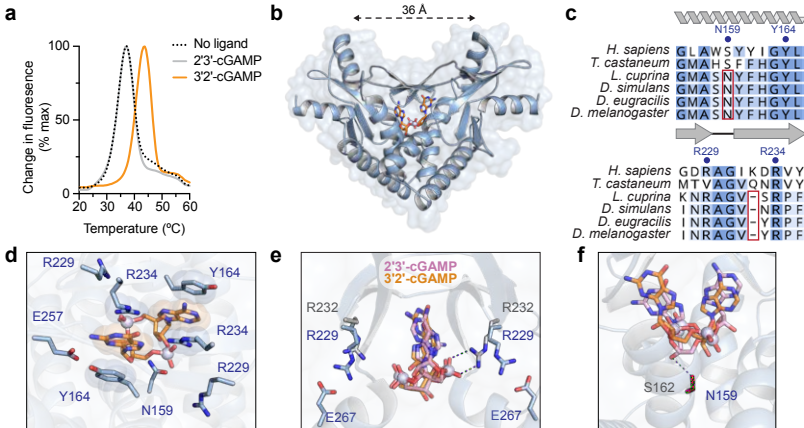
Fig. 5 | 3'2'-cGAMP activates STING-dependent antiviral immunity in *Drosophila*
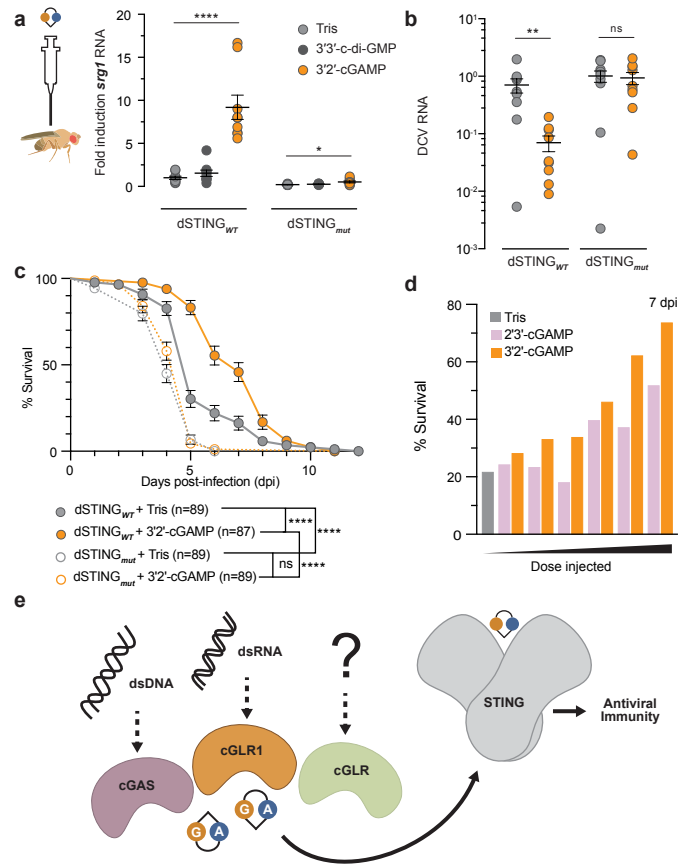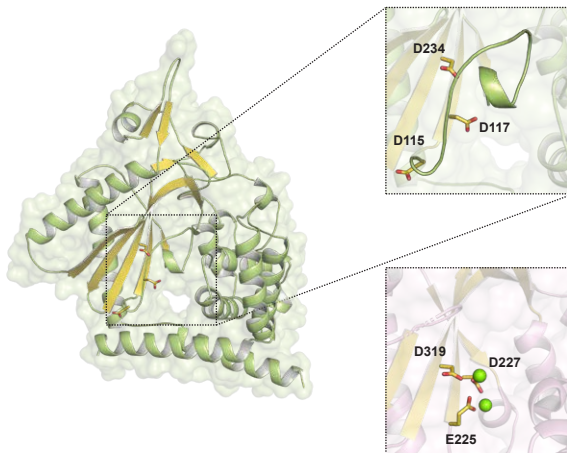
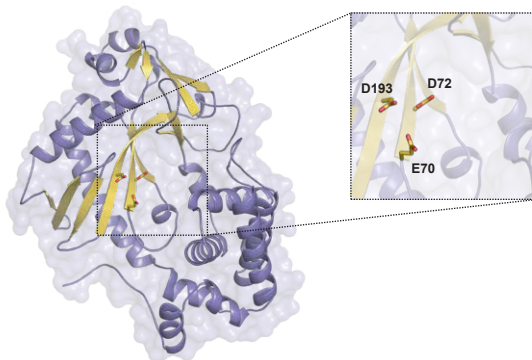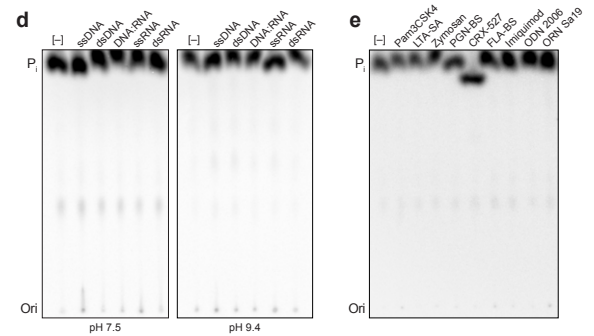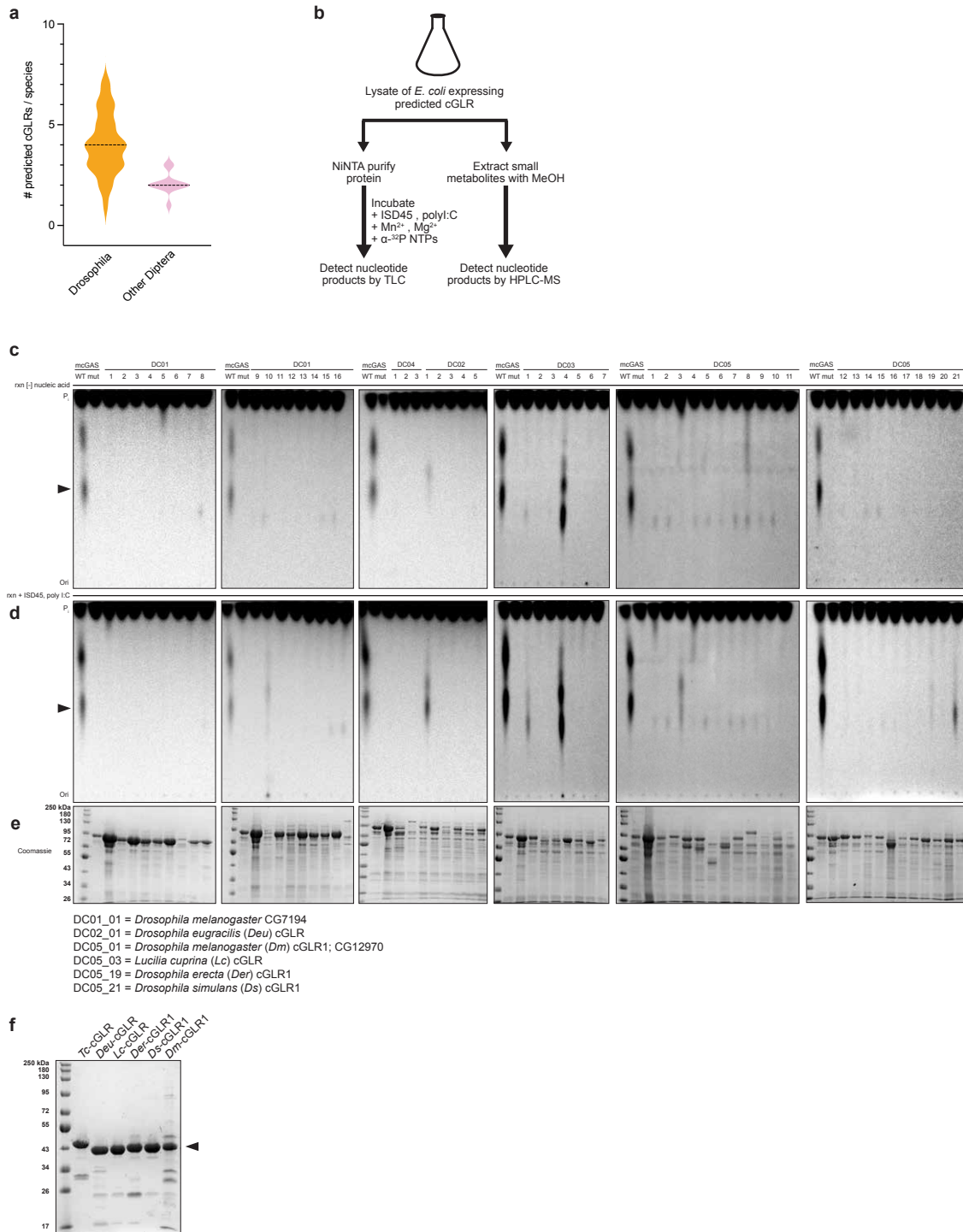**Extended Data Fig. 1 | Sequence and structural analysis of hMB21D2 and *Tc*-cGLR**
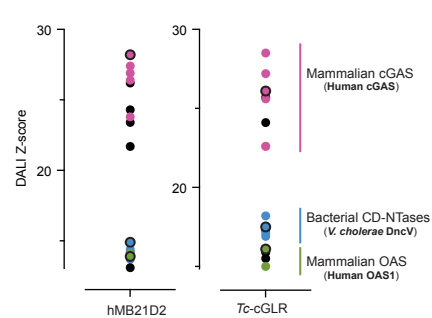
Extended Data Fig. 2 | Forward biochemical screen of predicted cGLRs in *Diptera*

DC01_01 = *Drosophila melanogaster* CG7194
DC02_01 = *Drosophila eugracilis* (*Deu*) cGLR
DC05_01 = *Drosophila melanogaster* (*Dm*) cGLR1; CG12970
DC05_03 = *Lucilia cuprina* (*Lc*) cGLR
DC05_19 = *Drosophila erecta* (*Der*) cGLR1
DC05_21 = *Drosophila simulans* (*Ds*) cGLR1

Extended Data Fig. 3 | Sequence analysis and mutagenesis of insect cGLRs

a

b *Ds*-cGLR1

c *Ds*-cGLR1   *Tc*-cGLR

d

e *Tc*-cGLR modeled with dsRNA

f
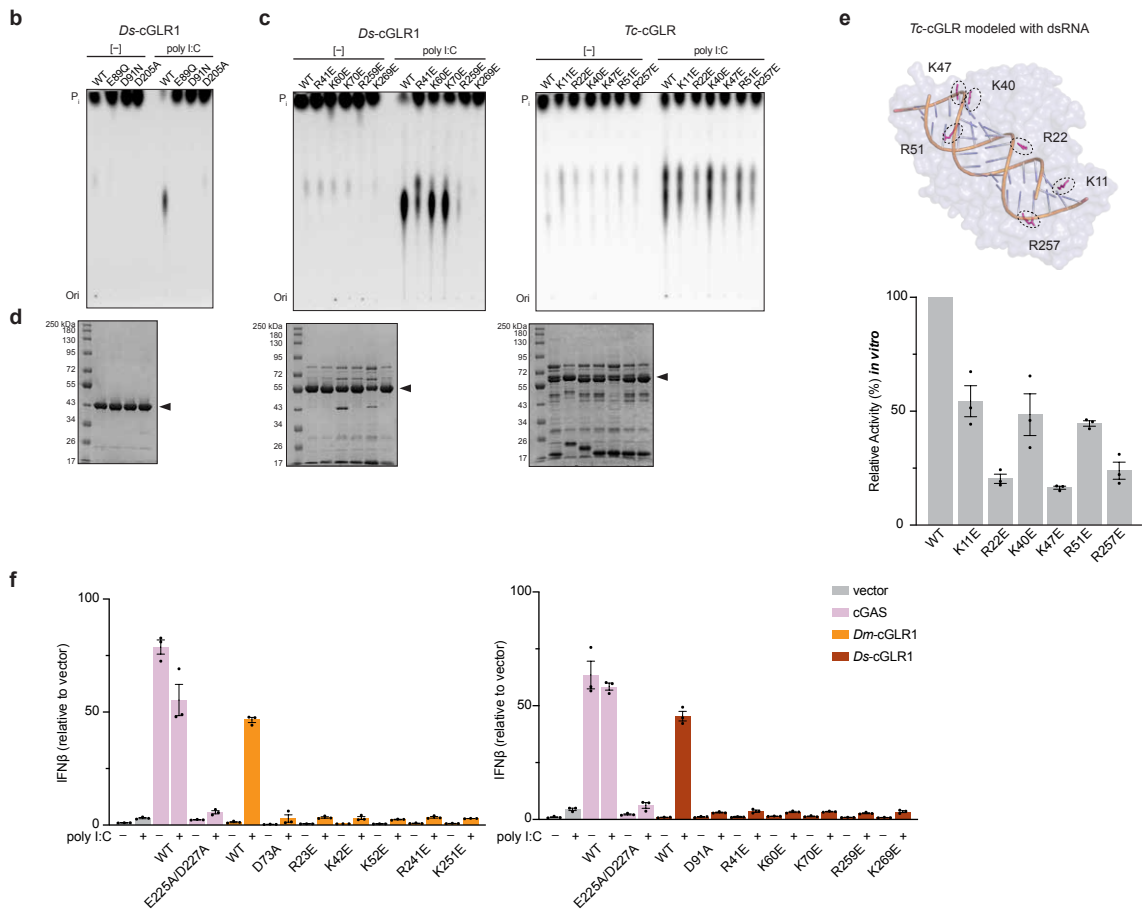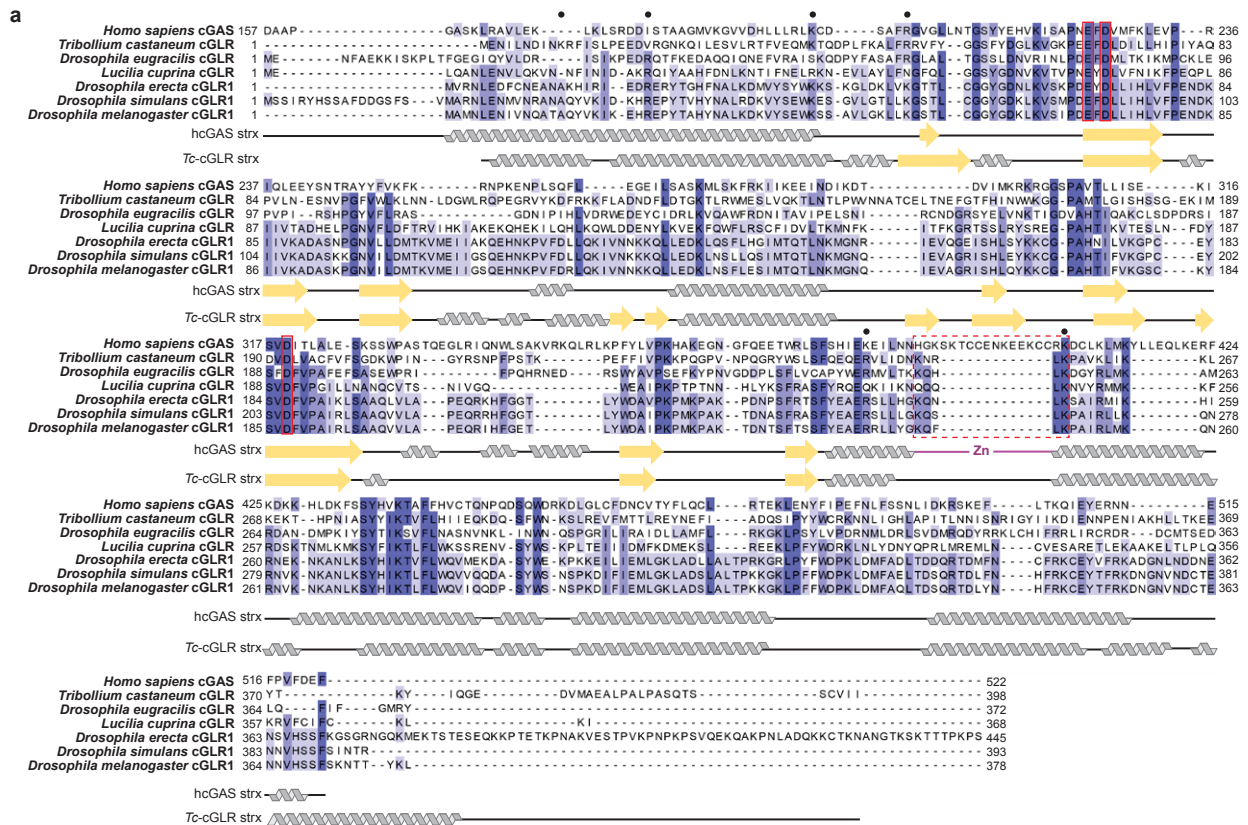
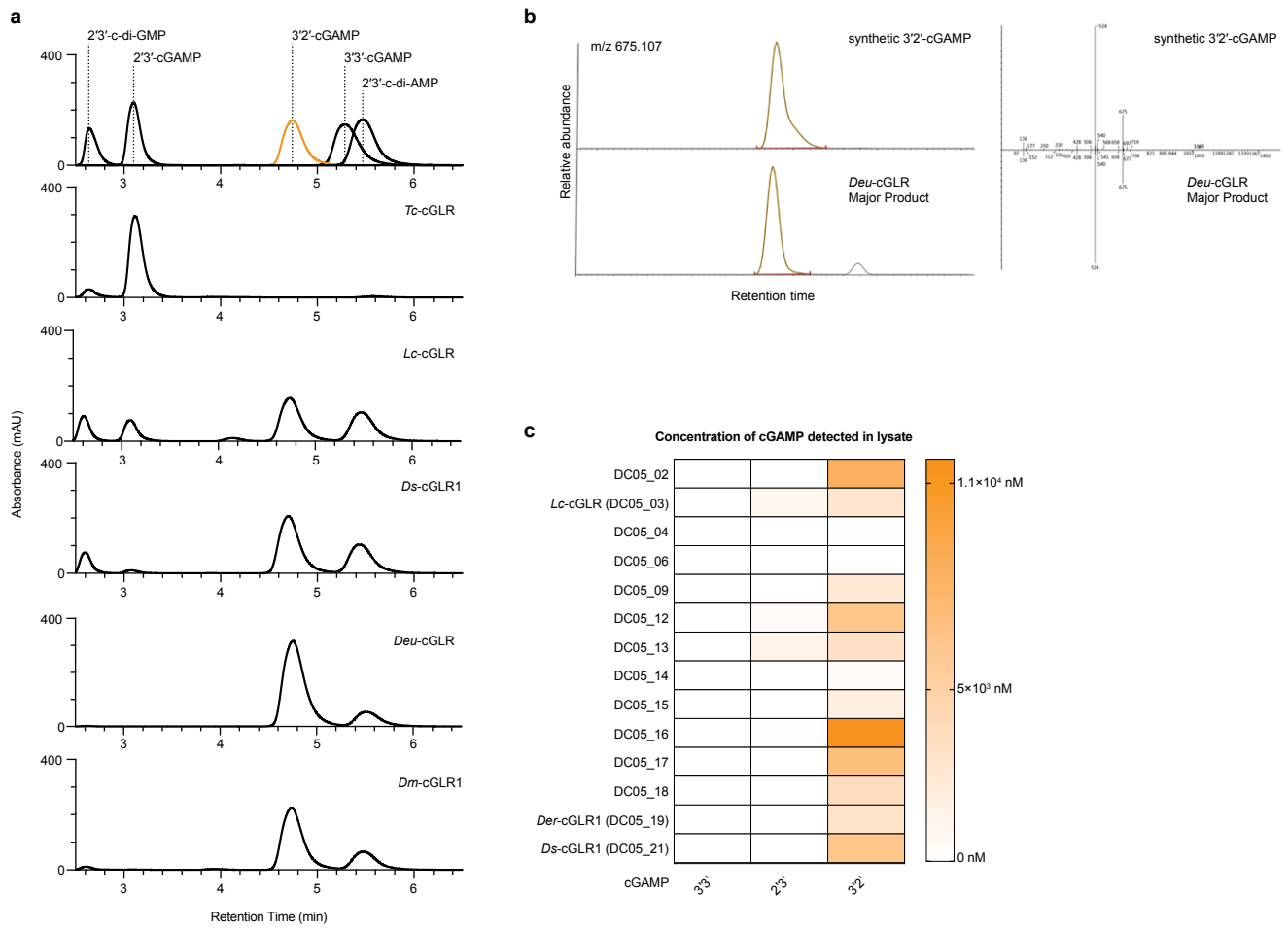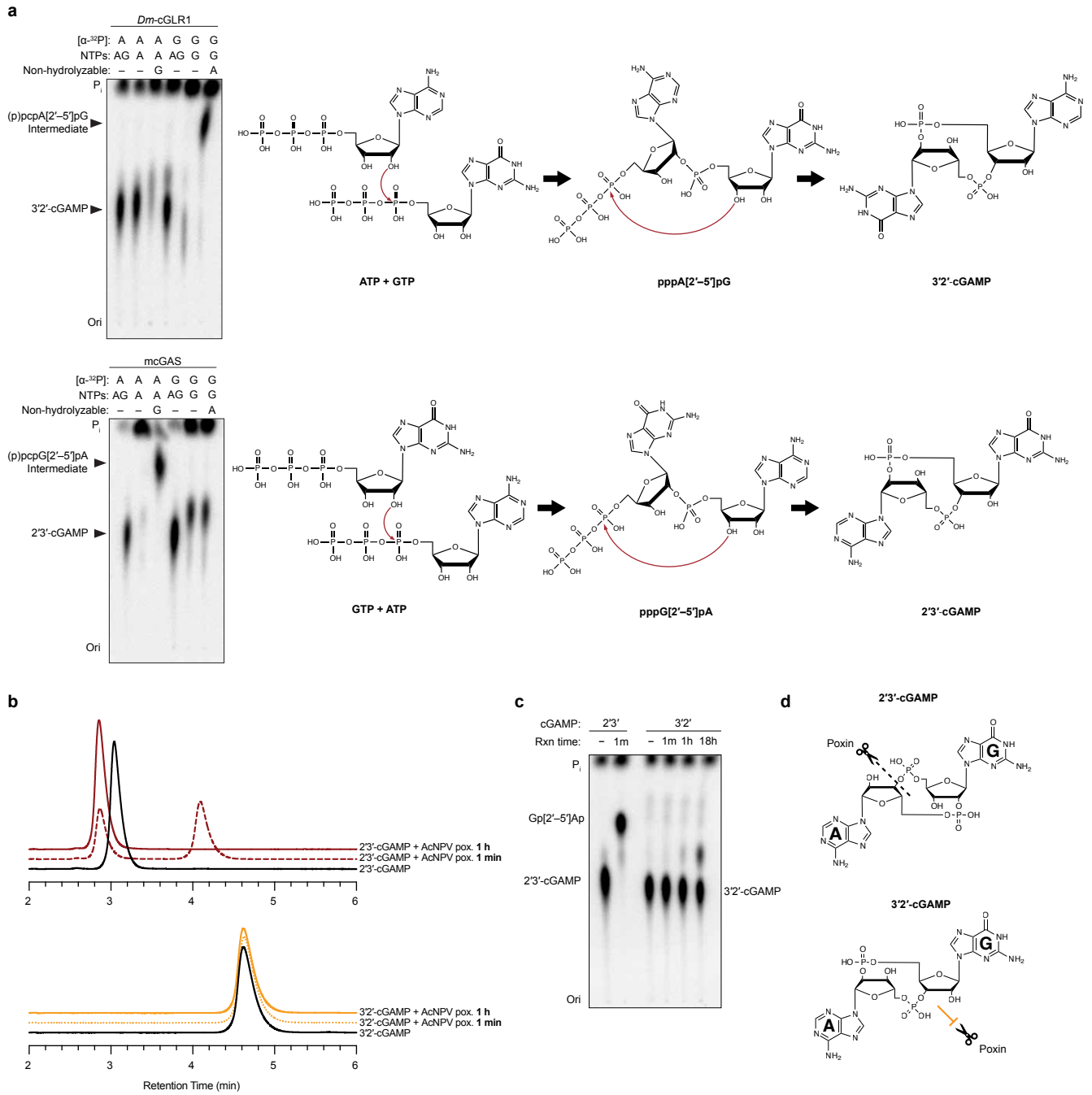**Extended Data Fig. 4 | Analysis of RNA-recognition by insect cGLRs**
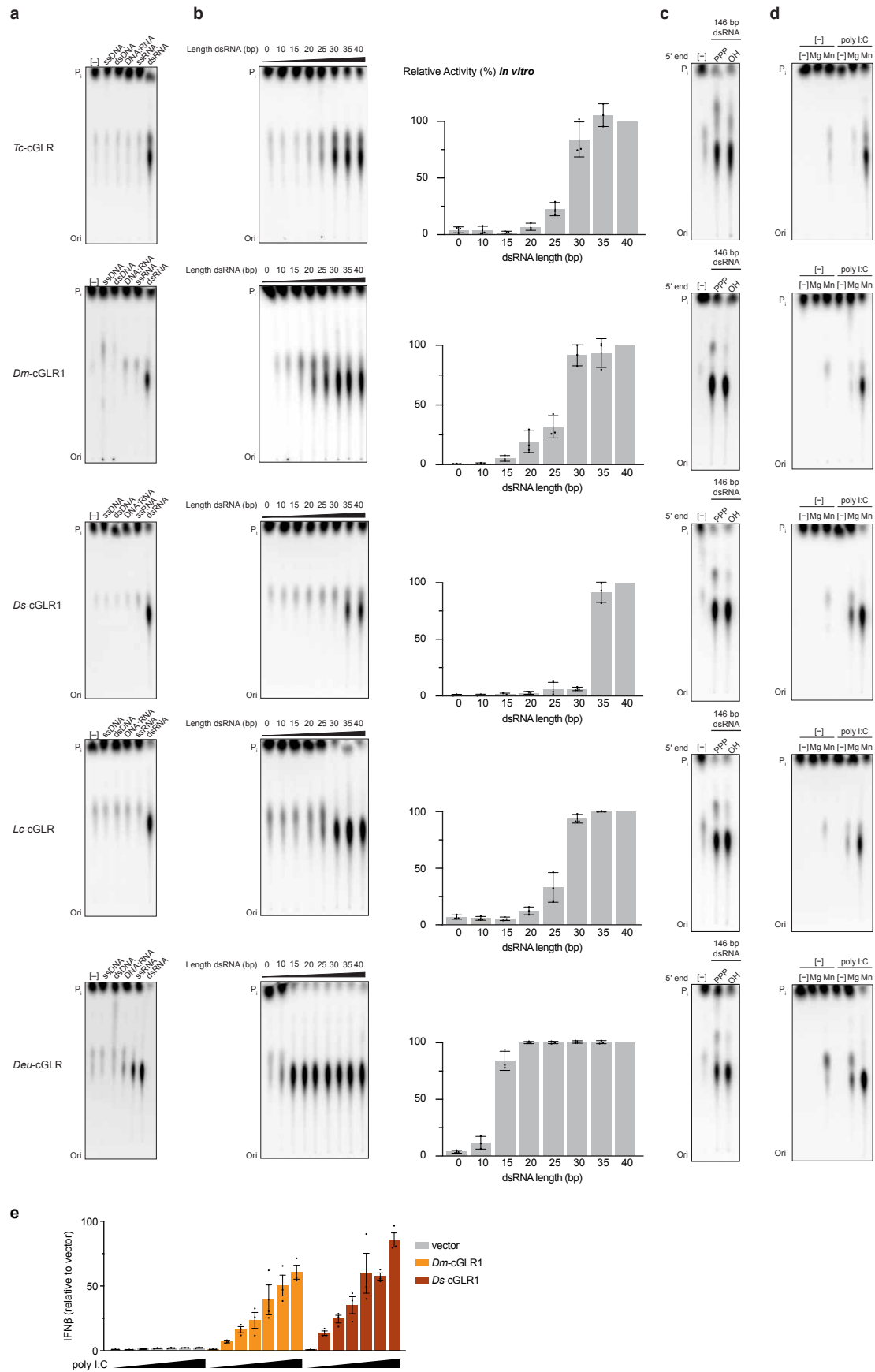
Extended Data Fig. 5 | Characterization of *Ds*-cGLR1–dsRNA condensate formation
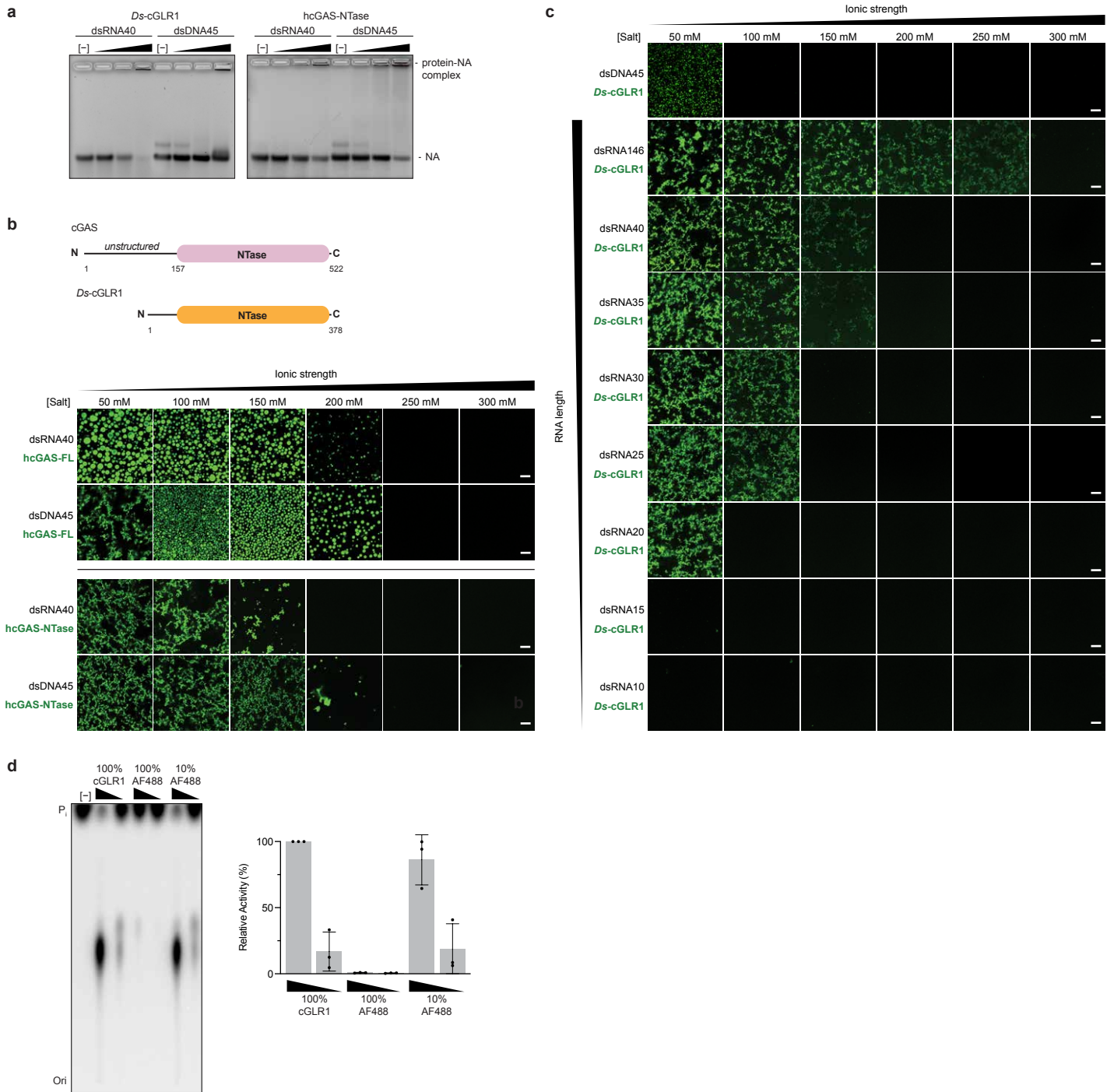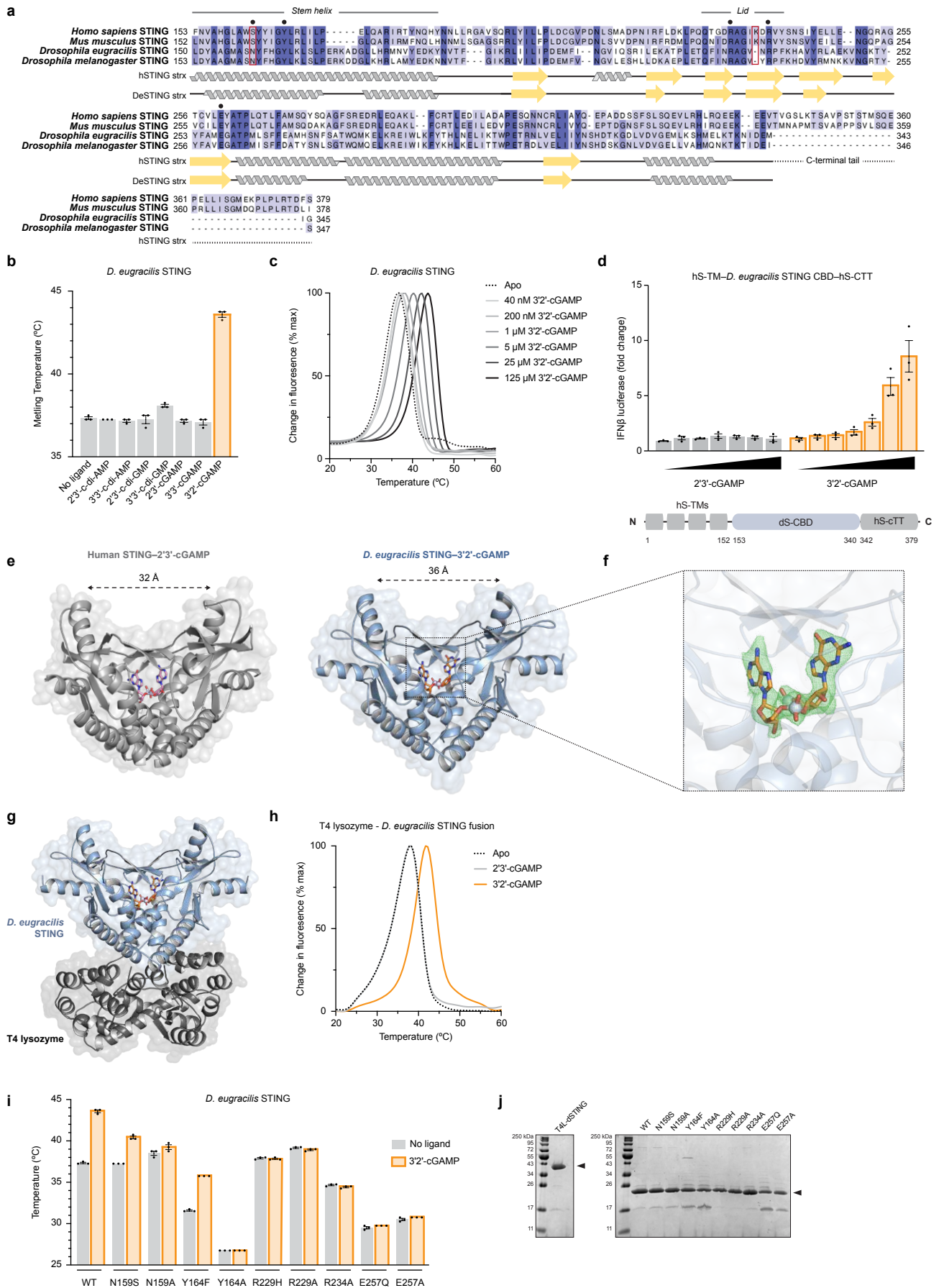
Extended Data Fig. 6 | Synthesis of 3′2′-cGAMP by *Diptera* cGLRs

a

b

c
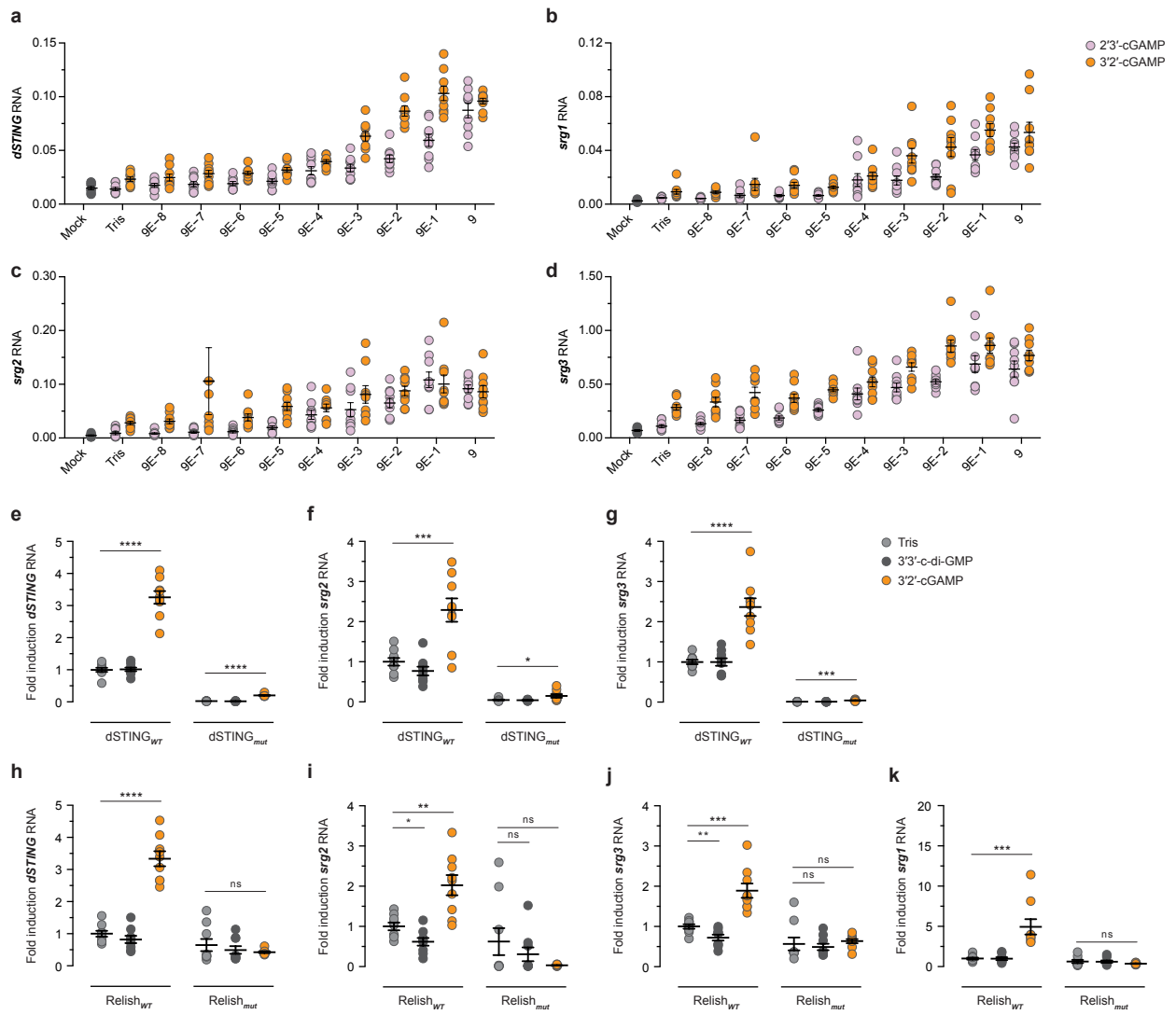Concentration of cGAMP detected in lysate

Extended Data Fig. 7 | Mechanism of 3′2′-cGAMP bond formation and resistance to degradation by viral poxin enzymes

Extended Data Fig. 8 | Structural and biochemical analysis of *Drosophila* STING

Extended Data Fig. 9 | 3′2′-cGAMP induces the expression of dSTING-regulated genes

Extended Data Fig. 10 | 3′2′-cGAMP functions as a potent antiviral ligand